Interactions between Water Vapor and Potential Vorticity in Synoptic-Scale Monsoonal Disturbances: Moisture Vortex Instability

ÁNGEL F. ADAMES[a]

NOAA/Geophysical Fluid Dynamics Laboratory, Princeton, New Jersey, and University Corporation for Atmospheric Research, Boulder, Colorado

YI MING

NOAA/Geophysical Fluid Dynamics Laboratory, Princeton, New Jersey

(Manuscript received 13 October 2017, in final form 9 March 2018)

ABSTRACT

South Asian monsoon low pressure systems, referred to as synoptic-scale monsoonal disturbances (SMDs), are convectively coupled cyclonic disturbances that are responsible for up to half of the total monsoon rainfall. In spite of their importance, the mechanisms that lead to the growth of these systems have remained elusive. It has long been thought that SMDs grow because of a variant of baroclinic instability that includes the effects of convection. Recent work, however, has shown that this framework is inconsistent with the observed structure and dynamics of SMDs. Here, we present an alternative framework that may explain the growth of SMDs and may also be applicable to other modes of tropical variability. Moisture is prognostic and is coupled to precipitation through a simplified Betts–Miller scheme. Interactions between moisture and potential vorticity (PV) in the presence of a moist static energy gradient can be understood in terms of a "gross" PV (q_G) equation. The q_G summarizes the dynamics of SMDs and reveals the relative role that moist and dry dynamics play in these disturbances, which is largely determined by the gross moist stability. Linear solutions to the coupled PV and moisture equations reveal Rossby-like modes that grow because of a moisture vortex instability. Meridional temperature and moisture advection to the west of the PV maximum moisten and destabilize the column, which results in enhanced convection and SMD intensification through vortex stretching. This instability occurs only if the moistening is in the direction of propagation of the SMD and is strongest at the synoptic scale.

1. Introduction

Synoptic-scale variability in the tropics is governed by a variety of disturbances that couple to convection. Among the least understood of these disturbances are cyclonic features that occur during the active months of the Indian monsoon. These disturbances are known as monsoon low pressure systems, or synoptic-scale monsoonal disturbances (SMDs). These systems exhibit a horizontal scale of ~2000 km (Godbole 1977; Krishnamurti et al. 1975; Sikka 1977; Lau and Lau 1990) and circulation anomalies that are strongest in the lower troposphere (Cohen and Boos 2016; Hunt et al. 2016; Adames and Ming 2018). SMDs also exhibit significant precipitation anomalies, which are a maximum to the west or southwest of the center of low pressure (Mooley 1973; Yoon and Chen 2005; Hunt et al. 2016). SMDs predominantly develop over the Bay of Bengal, propagate northwestward toward the Indian subcontinent with a phase speed of ~5 m s^{-1} (Mooley 1973; Godbole 1977; Krishnamurti et al. 1975, 1976; Sikka 1977; Hunt and Turner 2017). As they propagate northwestward, they produce a large fraction of the total monsoonal rainfall received by India (Stano et al. 2002; Ding and Sikka 2006; Yoon and Chen 2005; Yoon and Huang 2012). The influence of SMDs on total monsoon precipitation indicates that understanding the mechanisms by which they propagate and grow is of central importance to our understanding of the South Asian monsoon.

Denotes content that is immediately available upon publication as open access.

[a] Current affiliation: Department of Climate and Space Science and Engineering, University of Michigan, Ann Arbor, Michigan.

Corresponding author: Ángel F. Adames, afadames@umich.edu

DOI: 10.1175/JAS-D-17-0310.1

It has long been thought that SMDs are destabilized by a variant of baroclinic instability (Charney and Stern 1962; Bretherton 1966) that is modified by diabatic heating, referred to ''moist baroclinic instability'' (Salvekar et al. 1986; Krishnakumar et al. 1992; Aravequia et al. 1995; de Vries et al. 2010; Krishnamurti et al. 2013). Similarly to the original dry baroclinic instability model, this moist model includes counterpropagating waves that can phase lock and induce mutual growth. For this phase locking to occur, the anomalies in potential vorticity (PV) must tilt against the climatological-mean vertical wind shear (de Vries et al. 2010; Cohen and Boos 2016). However, it was recently shown by Cohen and Boos (2016) that the structure of SMDs, as described by modern reanalysis products, is inconsistent with the criteria necessary for moist baroclinic instability to occur. For example, they found that SMDs exhibit an upright vertical structure, which is inconsistent with the tilting necessary for baroclinic instability to occur. Furthermore, Boos et al. (2015) found that the quasigeostrophic (QG) approximation, which is often employed in studies of monsoon low pressure systems (Subrahmanyam et al. 1981; Sanders 1984), does not sufficiently describe the dynamics of SMDs. These results suggest that other processes may be responsible for the growth of these systems.

In a recent study, Adames and Ming (2018) investigated the potential role that moist processes may have in SMDs simulated in GFDL's atmospheric general circulation model (AM4.0). They found a strong coupling between anomalous precipitation and column moisture. By jointly analyzing the moisture and moist static energy budgets, they found that the moisture anomalies propagate because of horizontal advection of mean dry static energy (DSE) by the anomalous winds. Horizontal advection of DSE induces a moisture tendency by forcing ascent along the sloping isentropes of the monsoon region. The anomalous precipitation is shifted ~5° to the east of the region of maximum ascent, where the moisture tendency is a maximum. This result suggests that the traditional QG assumption of forced ascent being tightly coupled to the precipitation field (Mak 1982; Sanders 1984) is incomplete, and moist thermodynamics may need to be included to fully explain the interaction between convection and the circulation in SMDs.

In this study, we propose a linear framework for SMDs. It incorporates a prognostic equation for column moisture, akin to the ''moisture mode'' framework commonly used to study the Madden–Julian oscillation (MJO; Fuchs and Raymond 2005, 2017; Raymond and Fuchs 2009; Sobel and Maloney 2012, 2013; Adames and Kim 2016). By incorporating a prognostic equation for column moisture, a wave instability arises that may describe the growth of SMDs. This instability involves a coupling between lower-tropospheric vorticity and column moisture. Warm-air and moisture advection by the anomalous winds moisten the free troposphere ahead of the cyclone, creating an environment favorable for deep convection. The subsequent convection intensifies the SMD through vortex stretching. The framework involves the use of equations reminiscent to those of the QG approximation but applied to the outer tropics ~16°N and with the addition of a prognostic moisture equation, which couples to precipitation through a linearized version of empirical relationship described by Bretherton et al. (2004).

While the focus of this study is on the growth and propagation of SMDs, we will show that it might be applicable to other modes of synoptic-scale tropical variability. Results from previous studies suggest that the same mechanism may operate in easterly waves both in the eastern Pacific and over Africa (Lau and Lau 1990, 1992; Kiladis et al. 2006; Serra et al. 2008; Berry and Thorncroft 2012; Janiga and Thorncroft 2013; Rydbeck and Maloney 2015) and monsoon depressions across the globe (Hurley and Boos 2015).

This paper is structured as follows. The next section offers a simple theoretical framework that can describe the structure and growth of SMDs. The dispersion relation of an idealized SMD is described in section 3. The role of precipitation in the growth of SMDs is discussed in section 4. Section 5 offers a simple equation that describes the zonal scale of SMDs. A discussion of the implications of the framework presented here is offered in section 6. A few concluding remarks are given in section 7.

2. A linear model for SMDs with prognostic moisture

In this section, we present a linear theoretical framework that can explain the growth and propagation of SMDs. We begin by presenting a basic set of equations linearized with respect to a background state with the following properties:

- Zonally uniform mean state that is characterized by a weak zonal flow
- A climatological-mean precipitation of ~10 mm day^{-1}
- The mean humidity and temperature increase with latitude

This mean state is chosen so that it qualitatively resembles the South Asian monsoon but is sufficiently simple to allow for solutions with a single-layer model. A more complete derivation and scaling of the basic

TABLE 1. Mean-state variables used in section 2.

Variable	Symbol	Definition	Value/units
Mean dry static energy	$\overline{s}$	$C_p\overline{T}+\overline{\Phi}$	J kg^{-1}
Mean column moisture	$\langle\overline{q}\rangle$	$\overline{\mathrm{RH}}\langle\overline{q}_s\rangle$	$49L_v$ J m^{-2}
Mean saturation column moisture	$\langle\overline{q}_s\rangle$	$\langle(0.622e_s)/[(p/100)-0.378e_s]\rangle$	$70L_v$ J m^{-2}
Mean column relative humidity	$\overline{\mathrm{RH}}$	$\langle\overline{q}\rangle/\langle\overline{q}_s\rangle$	0.70
Mean precipitation	$\overline{P}$	$P_0\exp(a_d\overline{\mathrm{RH}})$	240 W m^{-2}
Convective moisture adjustment time scale	τ_c	$\langle\overline{q}_s\rangle/(a_d\overline{P})$	1–12 h
Mean gross dry stability	$\tilde{M}_s$	$-\langle\Omega\partial\overline{s}/\partial p\rangle$	3.4×10^7 J m^{-2}
Mean gross moisture stratification	$\tilde{M}_q$	$\langle\Omega\partial\overline{q}/\partial p\rangle$	2.7×10^7 J m^{-2}
Normalized gross moist stability	$\tilde{M}$	$(\overline{M}_s-\overline{M}_q)/\tilde{M}_s$	0.2
Planetary vorticity at 16°N	f_0		4×10^{-5} s^{-1}
Planetary vorticity gradient	β	df/dy	2.2×10^{-11} m^{-1} s^{-1}
Meridional temperature gradient	β_T	$[(f_0C_p)/\tilde{M}_s]\langle\Lambda(\partial\overline{T}/\partial y)\rangle$	0.2×10^{-11} m^{-1} s^{-1}
Meridional moisture gradient	β_q	$[(f_0L_v)/M_q]\langle\Lambda(\partial\overline{q}/\partial y)\rangle$	0.8×10^{-11} m^{-1} s^{-1}
Meridional dry PV gradient	β_d	$\beta+\beta_T$	2.4×10^{-11} m^{-1} s^{-1}
Meridional moist PV gradient	β_m	$\beta_q+\beta_T$	1.0×10^{-11} m^{-1} s^{-1}
Meridional gross PV gradient	β_G	$\tilde{M}\beta_d+(1-\tilde{M})\beta_m$	$0–1\times10^{-11}$ m^{-1} s^{-1}
Free gravity wave phase speed	c	$[R_d\overline{M}_s/(C_p\langle a\rangle)]^{1/2}$	52 m s^{-1}
Rossby radius of deformation	L_d	c/f_0	1300 km
Inverse Rossby radius of deformation	k_d	$1/L_d$	7.7×10^{-7} m^{-1}
Vertical velocity basis function	Ω		Pa
Wind/geopotential basis function	Λ	$-\partial\Omega/\partial p$	Nondimensional
Temperature basis function	a	$\partial\Lambda/\partial\ln p$	Nondimensional

equations is shown in section a of the appendix. Variables and definitions used for the mean state are summarized in Table 1, while anomaly field variables are summarized in Table 2. The nomenclature used here closely follows the moisture mode treatments of the MJO described by Sobel and Maloney (2012, 2013) and Adames and Kim (2016).

The field variables are separated into time-mean (denoted by an overbar) and perturbation (denoted by a prime) components:

$$\Phi=\overline{\Phi}+\Phi', \tag{1}$$

where Φ is the geopotential. Perturbation fields are truncated vertically using basis functions, similar to the method of Neelin and Zeng (2000), Haertel et al. (2008), and Adames and Kim (2016):

$$\Phi'(x,y,p,t)=\phi'(x,y,t)\Lambda(p), \tag{2}$$

where the capital Φ' denotes the four-dimensional geopotential, the lowercase ϕ' denotes the vertically truncated geopotential, and Λ is the structure function for the wind and geopotential fields. Other field variables follow a similar truncation, described in section b of the appendix. All the structure functions used in this study are chosen so that they are consistent with a first baroclinic mode in vertical motion, a profile of ascent that is of the same polarity throughout the troposphere with a peak amplitude in the midtroposphere (~400 hPa).

The basic equations are vertically integrated in order to explicitly represent diabatic heating in terms of a precipitation rate P. The vertically integrated water vapor q is defined as

$$\langle q\rangle=\frac{1}{g}\int_{p_t}^{p_s}q\,dp, \tag{3}$$

where $g=9.8\,\mathrm{m\,s^{-2}}$ is the gravitational acceleration, $p_t=100$ hPa, and $p_s=1000$ hPa. Other variables are vertically integrated in the same way. The vertically truncated and integrated basic equations are analogous to shallow-water equations. This simplifies our equations significantly but has the caveat that vertical variations in the system are not included.

Interactions between column water vapor and precipitation may play a key role in the development and sustenance of SMDs. It was found by Hunt et al. (2016) that precipitation in SMDs is collocated with enhanced convective available potential energy (CAPE). They found that the enhanced CAPE is due to increased lower-tropospheric (upper boundary layer and lower free troposphere) moisture elevating the equivalent potential temperature of rising parcels. Similarly, Adames and Ming (2018) found that column moisture and precipitation are highly correlated in space in SMDs simulated by GFDL's AM4.0. This correlation is consistent with the notion that precipitation is an exponential function of column relative humidity RH, as described by Bretherton et al. (2004):

TABLE 2. Basic variables and definitions corresponding to the anomaly fields in section 2.

Variable	Symbol	Definition	Units
Column latent energy anomaly	$\langle q' \rangle$	$\int_{100\text{hPa}}^{1000\text{hPa}} q'\, dp/g$	J m^{-2}
Precipitation anomaly	P'	$\langle q' \rangle \tau_c^{-1}$	W m^{-2}
Anomalous streamfunction	ψ'		m^2 s^{-1}
Dry potential vorticity	q'_d	$\nabla^2\psi' - k_d^2\psi'$	s^{-1}
Moist potential vorticity	q'_m	$\tau_c f_0 P' \overline{M}_q^{-1} - k_d^2\psi'$	s^{-1}
Gross potential vorticity	q'_G	$\tilde{M} q'_d + (1-\tilde{M}) q'_m$	s^{-1}
Vorticity anomaly	ζ'	$\nabla^2\psi'$	s^{-1}
Horizontal divergence anomaly	D'	$\nabla \cdot \mathbf{v}'$	s^{-1}
Truncated horizontal wind anomaly	$\mathbf{v}'$	(u', v')	m s^{-1}
Truncated geopotential anomaly	ϕ'	$f_0\psi'$	m^2 s^{-2}
Truncated temperature anomaly	τ'	$-f_0\psi'/R_d$	K
Zonal wavenumber	k	$2\pi/\lambda_x$	m^{-1}
Meridional wavenumber	l	$2\pi/\lambda_y$	m^{-1}
Wave frequency	ω		s^{-1}
Approximate dry phase speed	c^x_{pd}	$-\tilde{M}\beta_d/(\tilde{M}K + k_d^2)$	m s^{-1}
Approximate moist phase speed	c^x_{pm}	$-(1-\tilde{M})\beta_m/(\tilde{M}K + k_d^2)$	m s^{-1}
Approximate zonal phase speed	c^x_p	$\omega/k = c^x_{\text{pm}} + c^x_{\text{pd}}$	m s^{-1}
Approximate zonal group velocity	c^x_g	$\partial\omega/\partial k$	m s^{-1}

$$P = P_0 \exp(a_d \times \text{RH}), \tag{4}$$

where P_0 and a_d are empirical constants and RH = $\langle q \rangle / \langle q_s \rangle$, where $\langle q_s \rangle$ is the saturation column water vapor. Following Adames (2017), we can linearize this curve with respect to a climatological-mean precipitation $\overline{P}$, from which we can obtain the following relation for the precipitation anomalies:

$$P' = a_d \overline{P} \frac{\langle q' \rangle}{\overline{\langle q_s \rangle}}, \tag{5}$$

where anomalies in column relative humidity are, to first order, due to anomalies in column water vapor (RH$'$ = $\langle q' \rangle / \langle \overline{q}_s \rangle$). We have neglected perturbations in $\langle q_s \rangle$ because they are much smaller than its mean value (see section a of the appendix). Note that, following Neelin and Zeng (2000) and Adames and Kim (2016), q and P will be implicitly scaled by the latent energy of vaporization L_v, so that $\langle q \rangle$ is in units of J m^{-2} and P in units of W m^{-2}. We can write Eq. (5) in terms of a convective moisture adjustment time-scale τ_c, akin to a simplified Betts–Miller scheme (Betts and Miller 1986; Betts 1986; Frierson 2007):

$$\tau_c = \frac{\overline{\langle q_s \rangle}}{a_d \overline{P}}. \tag{6}$$

Here, τ_c describes the sensitivity of P to changes in $\langle q \rangle$ and decreases as $\overline{P}$ increases (Bretherton et al. 2004; Adames 2017; Rushley et al. 2018). Over the climatologically rainy areas of the tropics, P is highly sensitive to changes in $\langle q \rangle$, and thus τ_c is smaller. Estimated values of τ_c over the warm pool and South Asian monsoon range from 4 h to 1 day (Bretherton et al. 2004; Sugiyama 2009; Jiang et al. 2016; Adames and Ming 2018).

With the above approximations, the leading terms in the momentum, thermodynamic, and moisture equations on a beta plane are written as

$$\frac{\partial u'}{\partial t} = f_0 v' + \beta y v' - \frac{\partial \phi'}{\partial x}, \tag{7a}$$

$$\frac{\partial v'}{\partial t} = -f_0 u' - \beta y u' - \frac{\partial \phi'}{\partial y}, \tag{7b}$$

$$\frac{1}{c^2}\frac{\partial \phi'}{\partial t} = v' \frac{\beta_T}{f_0} - D' - \frac{P'}{\overline{M}_s}, \tag{7c}$$

$$\frac{\tau_c}{\overline{M}_q}\frac{\partial P'}{\partial t} = -v' \frac{\beta_q}{f_0} - D' - \frac{P'}{\overline{M}_q}, \tag{7d}$$

where u' and v' are the zonal and meridional wind anomalies, respectively; $D' = \nabla \cdot \mathbf{v}'$ is the anomalous lower-tropospheric horizontal divergence, obtained as the vertical truncation of the vertical velocity (see section b of the appendix); and ϕ' is the anomalous geopotential. The f_0 is the planetary vorticity at 16°N, a latitude where SMDs commonly develop (Boos et al. 2015), and β is the meridional gradient of planetary vorticity at 16°N. The $\overline{M}_s$ and $\overline{M}_q$ are the climatological-mean gross dry stability and the gross moisture stratification, respectively, defined as

$$\overline{M_s} = -\left\langle \Omega \frac{\partial \overline{s}}{\partial p} \right\rangle, \tag{8a}$$

$$\overline{M_q} = \left\langle \Omega \frac{\partial \overline{q}}{\partial p} \right\rangle, \tag{8b}$$

where Ω is the vertical structure of ascent and $\overline{s} = C_p \overline{T} + \overline{\Phi}$ is the mean dry static energy, where C_p is the specific heat of dry air. The $\overline{M_s}$ and $\overline{M_q}$ can be thought as the vertical gradients of dry static energy and moisture characteristic of a wave whose vertical velocity field has a structure described by Ω. Their definitions are as in Neelin and Zeng (2000) and Adames and Kim (2016). Both $\overline{M_s}$ and $\overline{M_q}$ are defined as positive quantities. The phase speed of first baroclinic free gravity waves c is defined as

$$c = \left(\frac{R_d \overline{M_s}}{C_p \langle a \rangle} \right)^{1/2}, \tag{9}$$

where R_d is the dry gas constant and a is the vertical structure function of temperature. The β_T and β_q are the climatological-mean meridional temperature and moisture gradients, respectively, scaled so that they are in the same units as β:

$$\beta_T = \frac{f_0 C_p}{\overline{M_s}} \left\langle \Lambda \frac{\partial \overline{T}}{\partial y} \right\rangle, \tag{10a}$$

$$\beta_q = \frac{f_0 L_v}{\overline{M_q}} \left\langle \Lambda \frac{\partial \overline{q}}{\partial y} \right\rangle. \tag{10b}$$

It can be shown that β_T is related to the mean vertical wind shear through the thermal wind equation:

$$\beta_T = \frac{k_d^2}{\langle a \rangle} \left\langle \Lambda \frac{\partial \overline{u}}{\partial \ln p} \right\rangle, \tag{11}$$

where $\overline{u}$ is the total mean zonal wind and k_d is the inverse of the Rossby radius of deformation L_d (Vallis 2017):

$$k_d = \frac{f_0}{c}. \tag{12}$$

The β_T is defined here as a small quantity ($\beta_T \ll \beta$) that contributes little to the thermodynamic balance and to the momentum equations. However, it will play an important role in the dynamics of idealized SMDs.

The terms on the right-hand sides (rhs) of Eqs. (7a) and (7b) are the Coriolis acceleration ($f_0 + \beta y$) and the pressure gradient force, respectively. The rhs terms in Eq. (7c) are the meridional advection of mean temperature by the anomalous winds, vertical DSE advection, and heating by latent heat release, respectively. Finally, the equation for column moisture, which is converted to a precipitation equation via Eq. (6), contains three terms on the rhs: horizontal advection of mean moisture by the anomalous winds, vertical moisture advection, and the loss of moisture through precipitation. The terms in Eqs. (7c) and (7d) have been rearranged so that their similarities are more readily apparent. Note that advection of the terms in Eqs. (7a)–(7d) by the mean flow are neglected. This is because of the weak flow required to maintain simplicity in the analysis sought here. While strong zonal winds would be consistent with the observed monsoonal mean state, they would imply a strong mean vertical wind shear that would require inclusion of terms such as vertical advection of zonal momentum, which significantly complicate our analysis. Equations (7a)–(7d) are similar to those of Sukhatme (2014) and Monteiro and Sukhatme (2016), who also looked at the effects of moisture in a shallow-water system.

We can differentiate Eqs. (7a) and (7b) with respect to y and x, respectively, and convert them into an anomalous relative vorticity equation:

$$\frac{\partial \zeta'}{\partial t} = -v'\beta - f_0 D'. \tag{13}$$

The rhs terms of Eq. (13) correspond to advection of planetary vorticity by the anomalous meridional flow and generation of vorticity by anomalous divergence (Sardeshmukh and Hoskins 1988). The term $\beta y D'$ has been dropped since, for small variations in y, its contribution to the vorticity budget is small.

To further simplify the equations, we will assume that the anomalous horizontal winds are approximately nondivergent ($\zeta' \gg D'$; see section a of the appendix) and thus can be expressed in terms of a streamfunction:

$$\zeta' = \nabla^2 \psi', \tag{14a}$$

$$v' \simeq \frac{\partial \psi'}{\partial x}. \tag{14b}$$

Similarly, the anomalous geopotential can be expressed in terms of ψ':

$$\phi' \simeq f_0 \psi'. \tag{14c}$$

Substituting ζ' and v' in Eqs. (13) and (7d) with Eqs. (14a) and (14b) reduces our set of variables to three. Finally, we can remove D' from the equations by merging Eqs. (7c) and (13) and similarly Eqs. (7c) and (7d) to create two equations with two variables. These equations are are the linear QG PV equation and the

moisture budget, respectively, the latter rewriten so that it is in units of vorticity:

$$\frac{\partial q_d'}{\partial t} = -v'\beta_d + \frac{f_0}{\overline{M_s}}P', \tag{15a}$$

$$\frac{\partial q_m'}{\partial t} = -v'\beta_m - \frac{f_0\tilde{M}}{\overline{M_q}}P', \tag{15b}$$

where

$$\tilde{M} = \frac{\overline{M_s} - \overline{M_q}}{\overline{M_s}} \tag{15c}$$

is the normalized vertical gross moist stability (NGMS; Neelin and Held 1987; Raymond et al. 2009), a measure of the effective static stability of the atmosphere,

$$q_d' = \nabla^2\psi' - k_d^2\psi' \tag{16a}$$

is the QG PV anomaly, and

$$q_m' = \frac{f_0\tau_c}{\overline{M_q}}P' - k_d^2\psi' \tag{16b}$$

can be thought as the PV that is generated from precipitation. We will refer to q_d' as the dry PV and q_m' as the moist PV. Similarly, we define the dry and moist PV gradients defined as

$$\beta_d = \beta + \beta_T, \tag{17a}$$

$$\beta_m = \beta_q + \beta_T. \tag{17b}$$

The rhs of Eq. (15a) are the advection of mean dry PV by the anomalous meridional flow and PV generation from vortex stretching in deep convection. The terms in Eq. (15b) are equivalent but corresponding to the moist PV field. In the moist PV (moisture) budget, however, only a negative NGMS results in generation of moist PV. When the NGMS is negative, vertical moisture import exceeds the loss of moisture through precipitation, thus allowing the moist PV anomalies to increase. The converse is true when the NGMS is positive. Equations (15a) and (15b) are reminiscent of Eqs. (30) and (31) in Smith and Stechmann (2017), and our equations can be thought as a shallow-water versions of their equations.

We can merge Eqs. (15a) and (15b) to remove P' from the rhs and obtain one equation that fully describes the idealized SMDs analyzed here:

$$\frac{\partial q_G'}{\partial t} = -v'\beta_G, \tag{18a}$$

where

$$\begin{aligned} q_G' &= \tilde{M}q_d' + (1-\tilde{M})q_m' \\ &= \tilde{M}\nabla^2\psi' - k_d^2\psi' + \frac{f_0\tau_c}{\overline{M_s}}P' \end{aligned} \tag{18b}$$

will be referred to as the "gross" PV and

$$\beta_G = \tilde{M}\beta_d + (1-\tilde{M})\beta_m \tag{18c}$$

is the mean gross PV gradient. The prefix "gross" implies a generalized PV field that includes vorticity generation from moist processes while also suggesting its relationship to NGMS. We use uppercase G as the subscript since lowercase g is commonly used to denote fields that are in geostrophic balance. A schematic comparing the gross PV framework with the dry PV framework is shown in Fig. 1.

Equations (18a)–(18c) describe the relative importance of dry and moist processes to the propagation of an idealized SMD. This relationship is demonstrated in Fig. 2 for fixed values of β_d and β_d, but it also applies to q_d' and q_m'. When the atmosphere is dry, the NGMS is approximately unity, and precipitation processes become negligible ($\tilde{M} \to 1$, $P' \to 0$, and $\beta_G \sim \beta_d$) so that Eq. (18a) becomes the equation for dry PV [Eq. (15a)]. When the atmosphere is moist ($\tilde{M} \to 0$), $\beta_G \sim \beta_m$, indicating that the propagation of the anomalous circulation is governed by moist processes (β_m). For values of $\tilde{M}$ between 0 and 1, both dry and moist processes contribute to the propagation of the wave, and their relative contributions depend on the values of these two terms, as shown in Fig. 2.

In the following section, it will be shown that unstable Rossby-like modes arise from the equations described in this section. This implies that the gross PV is not a materially conserved quantity. Nonetheless, it will be shown that it is a useful quantity for understanding the dynamics of SMDs.

3. Dispersion relation

In this section, we will seek linear wave solutions to the equations presented in the previous section. To do this, several additional approximations are required. Meridional variations in $\overline{M_s}$ and $\overline{M_q}$ can be shown to be small (see section a of the appendix) over our analysis domain, such that the value at the reference latitude (16°N) can be used. Thus, the NGMS will be treated as a constant. The convective moisture adjustment timescale τ_c will be a constant corresponding to the time scale at the reference latitude. This corresponds to a

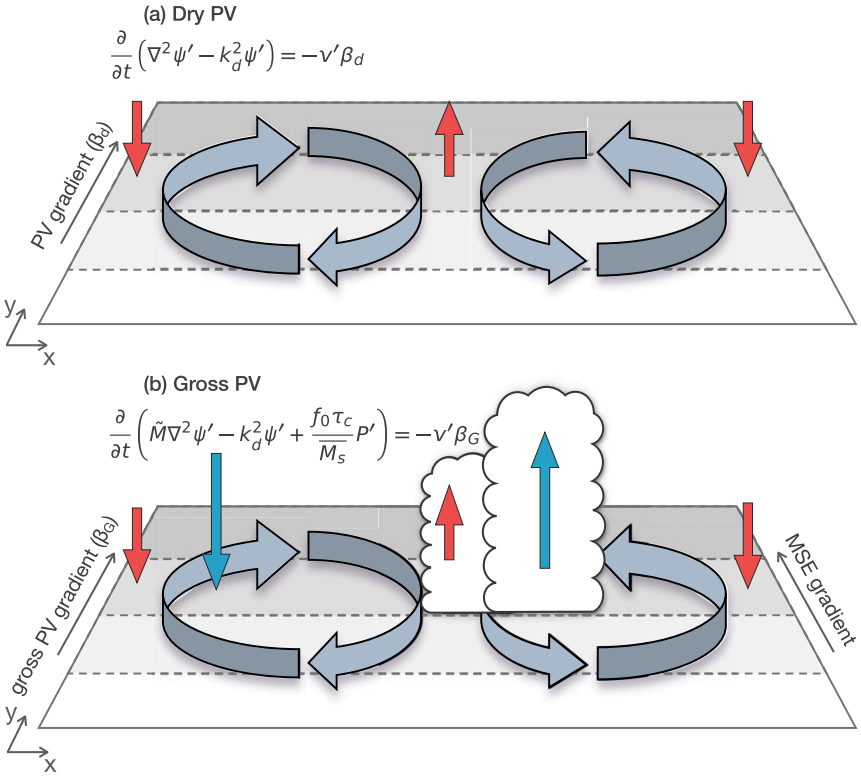

FIG. 1. Schematic describing the structure and propagation of (a) a dry Rossby wave and (b) an idealized SMD in the gross PV framework. In the dry PV framework, meridional advection of mean PV by the anomalous flow induces westward propagation of the Rossby wave. Isentropic (QG) ascent, denoted by a red arrow, occurs in phase with the northerly anomalies while descent occurs with southerly wind anomalies. The gross PV framework in (b) is a generization of (a) that includes meridional moisture gradient and the impact of moist processes in the PV budget. In it, horizontal moisture advection and QG ascent moisten the atmosphere. This moistening causes deep convection to increase (blue arrow), which results in a vorticity tendency from vortex stretching. The propagation of the wave is then from a combination of dry PV advection and vortex stretching from moist processes.

value of 12 h, which roughly corresponds to the average value of τ_c in the Asian monsoon. A value of 1 h will be used for approximate solutions, which corresponds to very high sensitivity of P to $\langle q \rangle$. Sensitivity of the idealized SMD solution to various values of τ_c and $\tilde{M}$ is shown in section d of the appendix.

a. Full solution

We can solve Eqs. (15a) and (15b) by assuming that they can be described by a wave of the form

$$\psi'(x,y,t) = \psi'_0 \exp(ikx + ily - i\omega t), \tag{19a}$$

$$P'(x,y,t) = P'_0 \exp(ikx + ily - i\omega t), \tag{19b}$$

where the subscript 0 refers to an initial perturbation of constant value, k and l are the zonal and meridional wavenumbers, respectively, and ω is the wave frequency.

By substituting Eqs. (19a) and (19b) onto Eqs. (15a) and (15b), we can solve the linear system of equations and obtain a dispersion relation. This is done by first solving for P' in Eq. (15b) and then substituting it in Eq. (15a), which yields

$$\omega[\tilde{M}K^2 + k_d^2 - i\tau_c\omega(K^2 + k_d^2) - i\tau_c\beta_d k] + \beta_G k = 0, \tag{20}$$

where $K^2 = k^2 + l^2$ is the horizontal wavenumber. Two solutions arise from this dispersion relation. The first solution is shown in Fig. 3a for $\tau_c = 12$ h. For $l = 0$, the frequency increases until zonal wavenumber 6 and steadily decreases for larger wavenumbers, reminiscinent of baroclinic Rossby waves. Growth, shown in Fig. 3c, is a maximum at the largest meridional scales and near zonal wavenumber 16. These modes exhibit meridionally elongated structures with little horizontal tilt. Damping is observed for zonal and meridional wavenumbers less

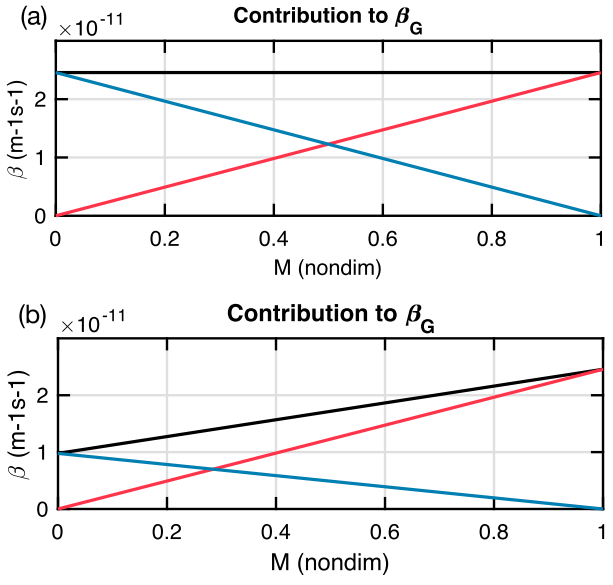

FIG. 2. Contributions of β_m and β_d to β_G as a function of the NGMS ($\tilde{M}$) for (a) $\beta_m = \beta_d = 2.4 \times 10^{-11}\,\mathrm{m^{-1}\,s^{-1}}$ and (b) $\beta_m = 1 \times 10^{-11}\,\mathrm{m^{-1}\,s^{-1}}$. Here, β_G is shown in black, β_m in blue, and β_d in red.

than 5. The dispersion relation for the second solution is shown in Figs. 3b and 3d. It is a slowly propagating wave that is strongly damped for all zonal and meridional wavenumbers. The rate of damping when averaged across all k and l in Fig. 3d is 0.6 day^{-1}. From here on, we will focus our discussion on the growing mode.

b. *Approximate solution*

An approximate dispersion relation can be obtained by considering the case when the imaginary component of Eq. (20) is small. We divide Eq. (20) by the terms in parentheses and then expand them into a Taylor series, truncating on the second term. This approximation is accurate for small values of τ_c, and we will discuss the resulting solution for a value of τ_c of 1 h. This may not be realistic, but it allows for some important insights that are still valid for larger values of τ_c. With this approximation, we obtain

$$\omega \simeq \frac{-\beta_G k}{\tilde{M}K^2 + k_d^2} - \frac{i\tau_c \beta_G k[\omega(K^2 + k_d^2) + \beta_d k]}{(\tilde{M}K^2 + k_d^2)^2}. \tag{21}$$

By rearranging the terms in Eq. (21) and expanding into a series once more, we obtain an approximate phase speed and group velocity of the form

$$c_p^x \simeq \frac{-\beta_G}{\tilde{M}K^2 + k_d^2}, \tag{22a}$$

$$c_g^x \simeq \frac{\beta_G(k_d^2 + \tilde{M}l^2 - \tilde{M}k^2)}{(\tilde{M}K^2 + k_d^2)^2}. \tag{22b}$$

This phase speed describes a Rossby wave whose propagation is determined by β_G rather than just β. Thus, both dry and moist processes contribute to the propagation of the wave. Following Cohen and Boos (2016), we can describe this phase speed as the sum of a dry component and a moist component:

$$c_p^x = c_{\mathrm{pd}}^x + c_{\mathrm{pm}}^x, \tag{23a}$$

$$c_{\mathrm{pd}}^x = \frac{-\tilde{M}\beta_d}{\tilde{M}K^2 + k_d^2}, \tag{23b}$$

$$c_{\mathrm{pm}}^x = \frac{-(1-\tilde{M})\beta_m}{\tilde{M}K^2 + k_d^2}. \tag{23c}$$

This separation allows us to more easily interpret the propagation of the idealized SMD. The c_{pd}^x is the component that is due to meridional dry PV advection. The moist phase speed is due to meridional moisture and temperature advection inducing increased precipitation to the west of the vortex. This component does not describe PV advection but PV generation due to vortex stretching that comes as a result of increased convection. The convection increases because of moistening from horizontal moisture advection (β_q) and vertical moisture advection that results from isentropic ascent (β_T).

Figure 4 shows the approximate zonal phase speed and group velocity of the approximate solution for the largest meridional scales and values of β_m ranging from 0 to $1 \times 10^{-11}\,\mathrm{m^{-1}\,s^{-1}}$. This corresponds to a temperature gradient that monotonically increases from 0 to 0.5 K (1000 km)$^{-1}$ and a moisture gradient that increases from 0 to 8 mm (1000 km)$^{-1}$. The wave exhibits westward phase propagation and a group velocity that is westward at the largest scales and eastward for smaller scales, and it is ~0 near zonal wavenumber 10, which is when $k = k_d\tilde{M}^{-1/2}$. As β_m increases, the phase speed increases, and the group velocity becomes more pronounced.

We can obtain a simple expression for the approximate growth rate by making use of the separation of c_p^x into dry (c_{pd}^x) and moist (c_{pm}^x) components, which yields

$$\mathrm{Im}(\omega) \simeq \frac{\tau_c k^2}{\tilde{M}} c_p^x c_{\mathrm{pm}}^x \left(1 + \frac{c_p^x k_d^2}{\beta_m}\right). \tag{24}$$

Figure 5 compares the approximate growth rate in Eq. (24) to the growth rate in Eq. (20). Nearly identical patterns are seen for $\tau_c = 1$ h. While the solution is less accurate for larger values of τ_c (not shown), growth is still a maximum near zonal wavenumber ~16.

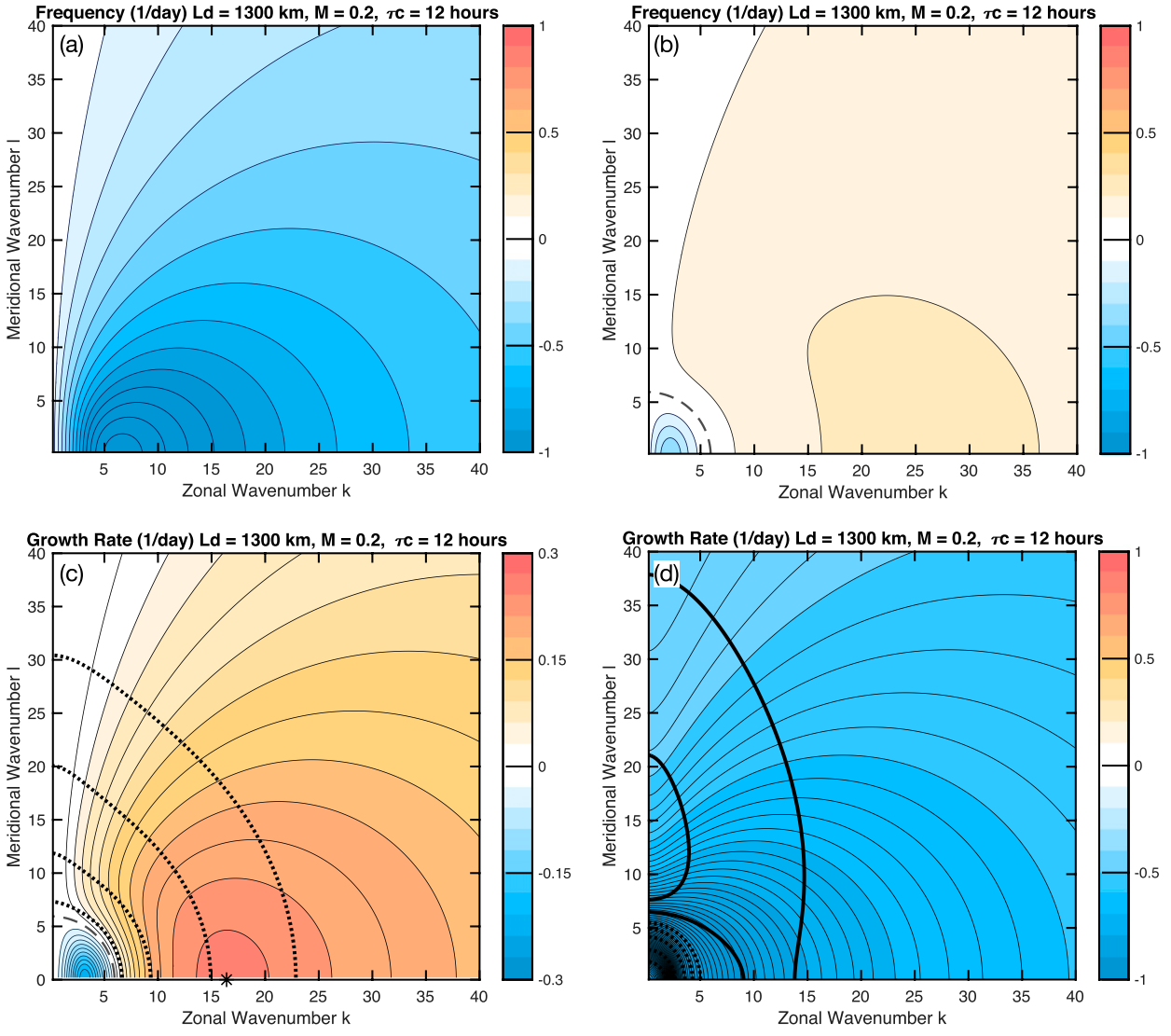

FIG. 3. Real component of the dispersion relation obtained from Eq. (20) for the (a) first and (b) second mode and the growth rate for the (c) first and (d) second mode. For all panels, $\tau_c = 12$ h, $\beta_m = 1 \times 10^{-11}\,\mathrm{m^{-1}\,s^{-1}}$, and $\beta_d = 2.4 \times 10^{-11}\,\mathrm{m^{-1}\,s^{-1}}$. Dotted lines correspond to constant phase speeds of -15, -10, -5, and $-2.5\,\mathrm{m\,s^{-1}}$, with decreasing values away from the origin. The location of maximum growth in (c) is denoted by an asterisk.

Figure 6a shows the growth rate for various values of β_m. When $\beta_m = 0$, the wave is weakly damped from zonal wavenumbers 0–30 and approximately neutral thereafter. For a small value of β_m of $2 \times 10^{-12}\,\mathrm{m^{-1}\,s^{-1}}$, the wave is unstable for zonal wavenumbers 15 and larger, and no clear scale selection is seen. For larger values of β_m, growth is largest at the synoptic scales, between zonal wavenumbers 10 and 25.

4. Precipitation and its relation to wave propagation and growth

The propagation and growth of the wave solution in the previous subsection can be elucidated by examining the relationship between q'_d and P'. Figure 7 shows q'_d, P', and the horizontal winds corresponding to a growing and a damped wave. In the growing wave, c_p^x and c_{pm}^x are both westward, implying that both β_G and β_m increase with latitude. As seen in Fig. 7b, both vortex stretching from convection and meridional dry PV advection are a maximum to the west of the q'_d maximum, which results in westward propagation. A salient feature of the growing wave solution is the phasing between P' and q'_d. As the wave propagates westward, P' increases and reaches a maximum amplitude at a time when the cyclonic anomalies exhibit an in-phase component with enhanced precipitation. This in-phase component of P' generates

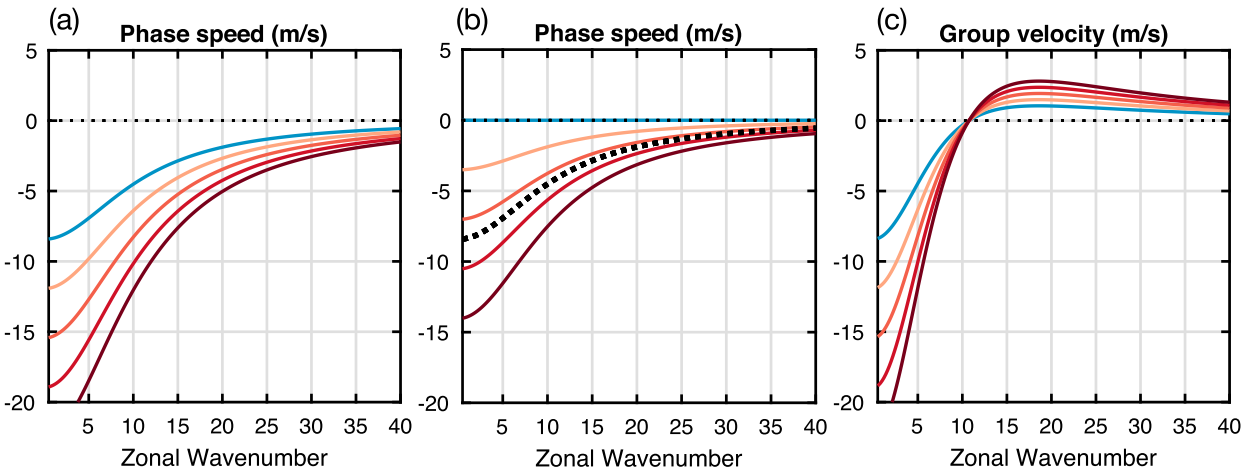

FIG. 4. (a) Approximate phase speed obtained from Eq. (22a) for $l = 0$, $L_d = 1300$ km, $\tilde{M} = 0.2$, and $\beta_d = 2.4 \times 10^{-11}\,\mathrm{m^{-1}\,s^{-1}}$. (b) Contributions to the total phase speed c_p^x from its dry (c_{pd}^x; dotted) and moist (c_{pm}^x; solid) contributions. In all panels, the blue line corresponds to $\beta_m = 0$, and darker shades or red indicate values of β_m of of 0.25, 0.5, 0.75, and $1 \times 10^{-11}\,\mathrm{m^{-1}\,s^{-1}}$. (c) As in (a), but showing the approximate group velocity as obtained from Eq. (22a).

additional cyclonic vorticity [Eq. (15a)], which causes the cyclonic anomalies to grow. Similarly, suppressed convection induces growth of the anticyclonic anomalies.

We can further elucidate the phase shifting of P' by examining the polarization relation between P' and ψ' (from which q_d' is defined), which can be written as follows:

$$P' = \frac{-i\overline{M}_q(\beta_m k + \omega k_d^2)}{f_0(\tilde{M} - i\omega\tau_c)}\psi'. \tag{25}$$

To understand the phasing between P' and ψ', it is convenient to convert Eq. (25) into an equation that describes the phase angle between P' and ψ'. By decomposing ω into its real ω_r and imaginary parts ω_i, we obtain the following:

$$\tan\alpha = -\frac{\tilde{M}(\beta_m k + \omega_r k_d) + \beta_m k\omega_i\tau_c}{\tau_c(\omega_r\beta_m k + \omega_r^2 k_d + \omega_i^2 k_d) + \tilde{M}\omega_i k_d}, \tag{26}$$

when P' and ψ' are of the same sign. When they are of the opposite sign, a value of π is added to the rhs of Eq. (26). A simpler relationship is obtained when we consider the case when the real component of the dispersion relationship is much larger than its imaginary part ($\omega_r \gg \omega_i$), which yields

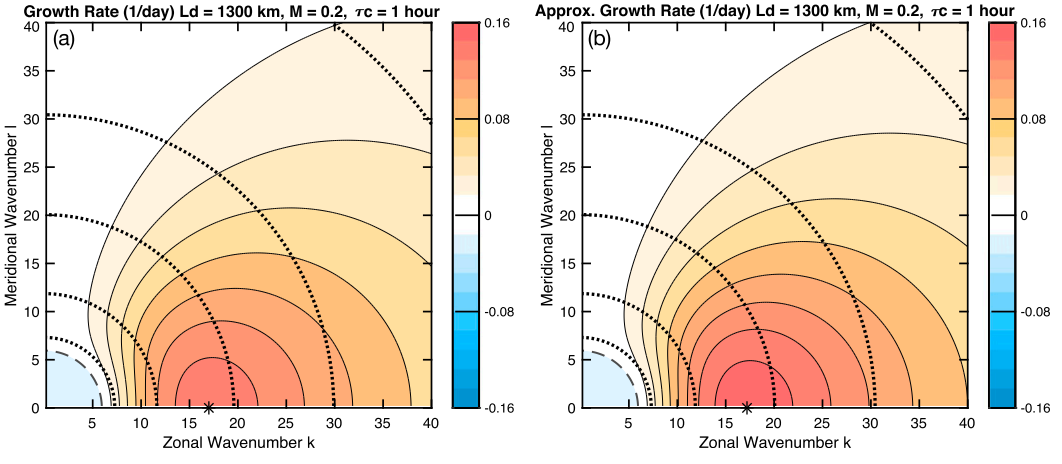

FIG. 5. (a) As in Fig. 3c, but for a value of τ_c of 1 h. (b) Approximate growth rate as obtained from Eq. (24). For both panels, $\beta_m = 1 \times 10^{-11}\,\mathrm{m^{-1}\,s^{-1}}$ and $\beta_d = 2.4 \times 10^{-11}\,\mathrm{m^{-1}\,s^{-1}}$. Dotted lines correspond to constant phase speeds of -15, -10, -5, -2.5, and $-1\,\mathrm{m\,s^{-1}}$, with decreasing values away from the origin. The location of maximum growth is denoted by an asterisk.

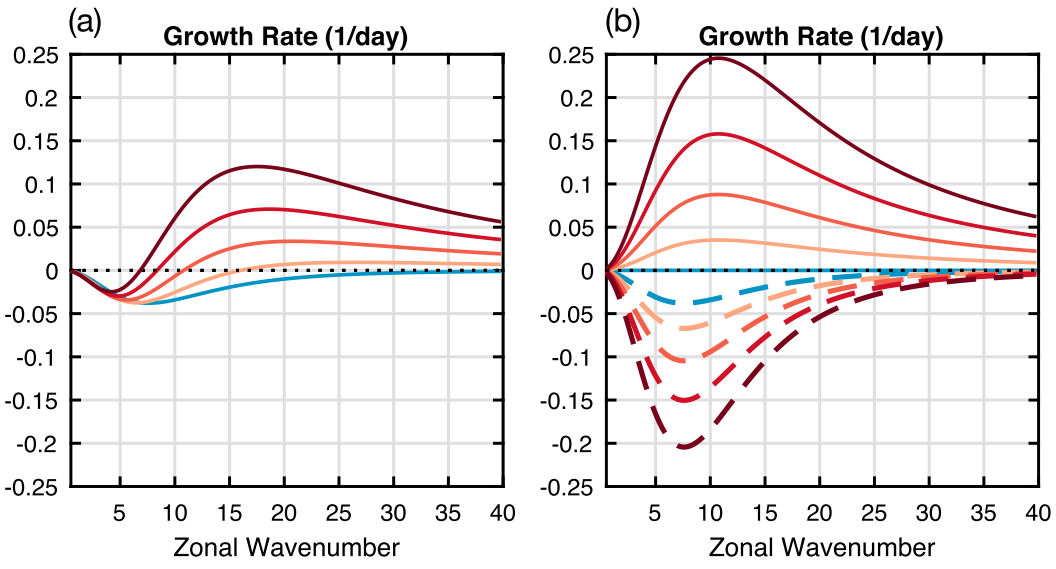

FIG. 6. (a) As in Fig. 4, but showing the approximate growth rate as defined in Eq. (24). (b) Contributions to the growth rate by the contribution from P'_A (solid) and the contribution from P'_T (dashed).

$$\tan\alpha \simeq -\frac{\tilde{M}}{\omega_r \tau_c}. \tag{27}$$

A schematic describing the phasing between P' and ψ', based on Eq. (27), is shown in Fig. 8. The interpretation is as follows. As the vortex propagates westward, the phasing between P' and ψ' depends on the duration of P' and the speed in which the circulation anomalies propagate. The P' is highly sensitive to $\langle q' \rangle$ when τ_c is small (~1 h) and responds quickly to moistening. Thus, small values of τ_c yield a P' response that is closely in phase with moistening, namely, horizontal advection of moist PV. When τ_c is long, the sensitivity is lower, and precipitation increases slowly, resulting in a shift toward the vortex center. The magnitude of the shifting also depends on the wave frequency since faster propagation will result in the wave propagating toward the region of precipitation more quickly. The relation to the NGMS can be understood as follows. When the NGMS is larger, moisture is removed quickly in a precipitating column, limiting the duration of precipitation. When the NGMS is small, moisture is removed slowly, allowing for longer duration of precipitation. Longer-lasting precipitation results in a larger shift toward the center of low pressure.

The phasing between P' and ψ' also depends on c_p and $c_{\rm pm}$, which determine the growth rate [Eq. (24)]. As shown in Fig. 7a, the wave grows when c_p and $c_{\rm pm}$ are in the same direction. Figure 7c shows the case in which c_p is westward but $c_{\rm pm}$ is eastward. Anomalous southerly flow now induces moistening, and precipitation is a maximum to the east of the moistening. This results in a P' that is slightly in phase with the anticyclonic anomalies. Because precipitation generates a cyclonic tendency, it follows that it will damp the anticyclonic anomalies.

From inspection of Eq. (25), we can define two different processes that contribute to precipitation, corresponding to the terms in parentheses in the numerator of Eq. (25). The first is the advection of moist PV by the anomalous winds, which we will refer to as the advective contribution P'_A. The second is related to the temperature tendency ($k_d\psi'$) term in Eq. (15b), which we will refer to as the thermal contribution P'_T. We can think of this term as the contribution to P' from vertical moisture advection from adiabatic ascent (descent) that occurs in regions of cooling (warming). Air rising adiabatically is associated with moistening, and compression is associated with drying. The total precipitation is due to the sum of these two processes $P' = P'_A + P'_T$.

Figure 9 shows the P anomalies from Fig. 7 decomposed into P'_A and P'_T. It is clear that P'_A is the leading-order term. It is associated with moistening to the west of the q'_d maximum. The P'_T is smaller and of the opposite sign to P'_A. This can be interpreted as adiabatic compression to the west of the q'_d maximum reducing tropospheric moistening. This separation of P' into P'_A and P'_T allows us to further interpret the approximate growth rate in Eq. (24). The terms in parentheses can be interpreted as the growth induced by P'_A and P'_T, respectively, and their contributions are shown in Fig. 6b. When c_p^x and $c_{\rm pm}^x$ are in the same direction, P'_A favors

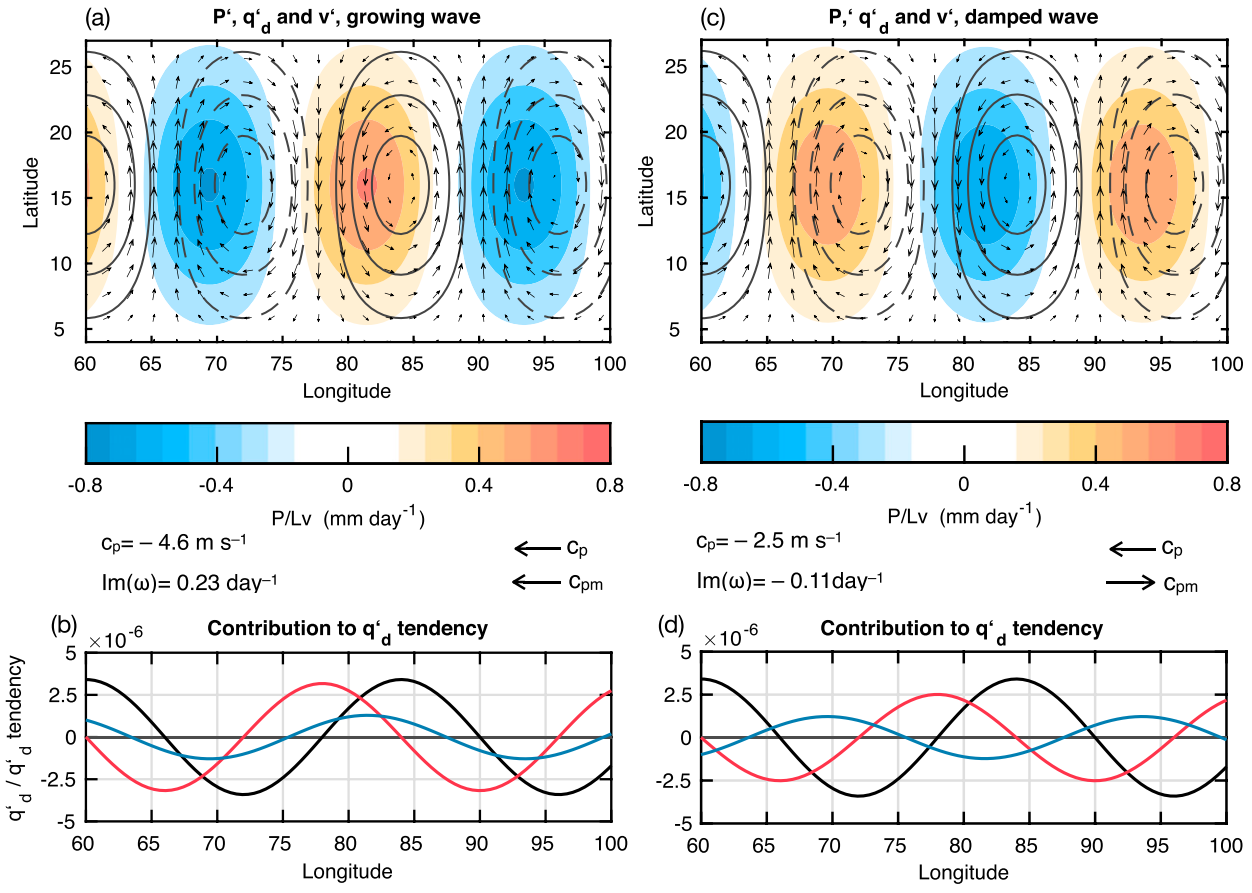

FIG. 7. Horizontal structure of an idealized SMD of zonal wavenumber 15 and a meridional structure that decays exponentially with the square of the distance from the reference latitude (16°N). The meridional decay is expressed through the formula $\exp[-(y-y_0)^2(5/3)k_d^2]$. (a),(b) The c_p^x and c_{pm}^x are westward; (c),(d) c_p^x is westward, and c_{pm}^x is eastward. In (a) and (c), precipitation is shown as the shaded field, q'_d in contours, and the surface horizontal wind as arrows. The largest arrows correspond to roughly 2 m s^{-1}. Contour interval is 2×10^{-6} s^{-1}. (b),(d) Curves indicate q'_d (black), meridional q'_d advection (red), and vortex stretching from precipitation (blue) meridionally averaged over the domain of (a) and (c) (4°–27°N). The q'_d is in units of s^{-1}, while the two other terms are in units of s^{-1} day^{-1}. The phase speed and growth rate are shown for each panel. For these plots, $\beta_T = 0.2\times10^{-11}$ m^{-1} s^{-1}, $\beta_q = 0.8\times10^{-11}$ m^{-1} s^{-1}, $\tilde{M}=0.2$, $\tau_c = 12$ h, and an initial streamfunction perturbation of $\psi_0 = 1\times10^6$ m^2 s^{-1}. The meridionally decaying structure is chosen such that the meridonal scale of the wave is much larger than the zonal scale, so it qualitatively represents the gravest meridional mode.

growth at all zonal wavenumbers and is a peak near zonal wavenumber 10. The P'_T, on the other hand, induces damping at all zonal wavenumbers and is a maximum near zonal wavenumber 7. When both terms are considered, the largest scales are damped and the maximum growth occurs at the synoptic scale.

The growing and damped modes can also be understood in terms of q'_G, as shown in Fig. 10. In the growing mode, q'_G is ~40% as large as q'_d and is shifted slightly to the east. This eastward shift implies that a small component of q'_G is in phase with the advection of β_G, implying that the wave is growing. In the damped mode (Fig. 10c), q'_G exhibits a smaller amplitude than the growing mode and is shifted to the east of q'_d. Advection of q'_G (β_G) is a maximum to the west of the q_G maximum, indicating westward propagation. An out-of-phase component is also clearly evident, suggesting that q'_G is damped. Thus, using q'_G offers a simple summary of the propagation and growth of these waves.

5. A qualitative relation for the SMD zonal scale

A qualitative relationship that describes the preferred scale of the idealized SMDs may be obtained by considering the case when $\tilde{M}\beta \ll (1-\tilde{M})\beta_m$, $\tilde{M}>0$, and $\tilde{M} \gg \omega\tau_c$ and by finding the zonal wavenumber $k_{\max}$, which satisfies $\partial \mathrm{Im}(\omega)/\partial k$. The approximation $\tilde{M}\beta \ll (1-\tilde{M})\beta_m$ implies that the propagation of the SMD is largely governed by moist processes and is reasonable for values of $\tilde{M}\sim 0.2$ and for $\beta_m \sim 1\times10^{-11}$ m^{-1} s^{-1}. In

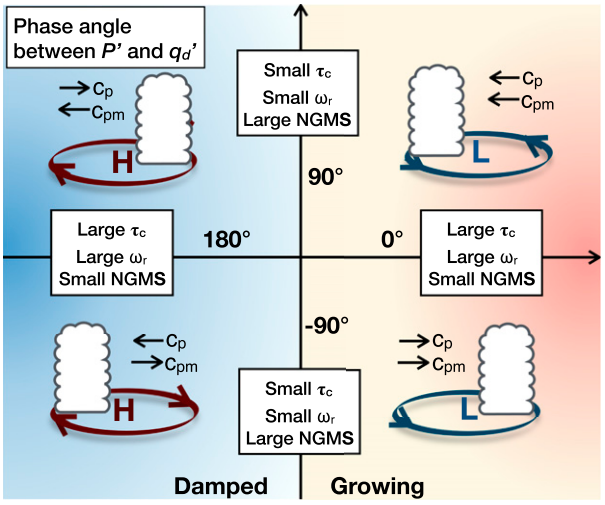

FIG. 8. Schematic describing the phase relationship between the circulation and precipitation for the wave solution in Eq. (20). For synoptic-scale waves, the phase angle can be broken down into four quadrants, the location which is determined by the direction of the total zonal phase speed c_p^x and the moist phase speed c_{pm}^x. The two left quadrants correspond to damped modes, while the two right quadrants correspond to growing modes. The displacement of the precipitation anomalies from the vortex center is determined by τ_c, ω_r, and the NGMS $\tilde{M}$. For large NGMS, small τ_c, or small ω_r, the precipitation anomalies are displaced away from the vortex center. Observed SMDs have a phasing corresponding to the top-right quadrant.

this case, the scale of the wave is approximately determined by the following simple relationship:

$$k \sim k_d \left(\frac{2}{\tilde{M}}\right)^{1/2}; \tag{28}$$

that is, the scale of idealized SMDs is proportional to the Rossby radius of deformation times the square root of half the NGMS [$\lambda_x \sim 2\pi L_d(\tilde{M}/2)^{1/2}$]. For values of k_d and $\tilde{M}$ used here (see Table 1), Eq. (28) yields a zonal wavelength of roughly 2600 km for our most unstable mode, which is similar to the observed wavelength of SMDs (Krishnamurti et al. 1975; Sikka 1977; Lau and Lau 1990).

6. Synthesis and discussion

In this study, we presented a linear framework that may explain the propagation and growth of SMDs. Based on results from recent observational and modeling studies (Hunt et al. 2016; Adames and Ming 2018), we propose that column moisture plays a central role in SMDs. By including a prognostic moisture equation and coupling it to precipitation through a simplified Betts–Miller scheme, we derive a dispersion that describes the following features of SMDs, including

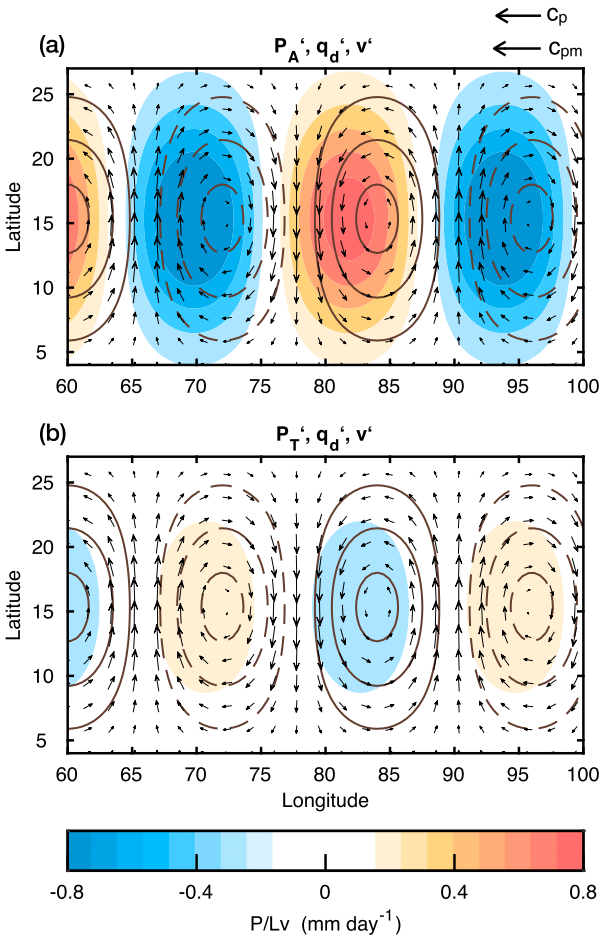

FIG. 9. As in Fig. 7a, but with (a) P'_A, the contribution to precipitation from moist PV advection, and (b) the contribution to precipitation P'_T, the contribution from the anomalous vertical motion that is associated with adiabatic expansion and compression.

- propagation mechanism,
- instability and growth, and
- synoptic scale (wavelengths of 2000–3000 km).

The instability occurs only if the wave's dry and moist phase speeds are in the same direction. The dry phase speed includes dry processes such as advection of planetary vorticity by the anomalous winds and vortex stretching from dry isentropic ascent. The moist phase speed only includes propagation that is induced by vortex stretching from deep convection. This stretching is a result of isentropic ascent and horizontal moisture advection moistening the free troposphere. These processes produce an instability by producing an environment conducive to deep convection. This subsequent convection occurs in phase with the cyclonic anomalies, intensifying them through vortex stretching.

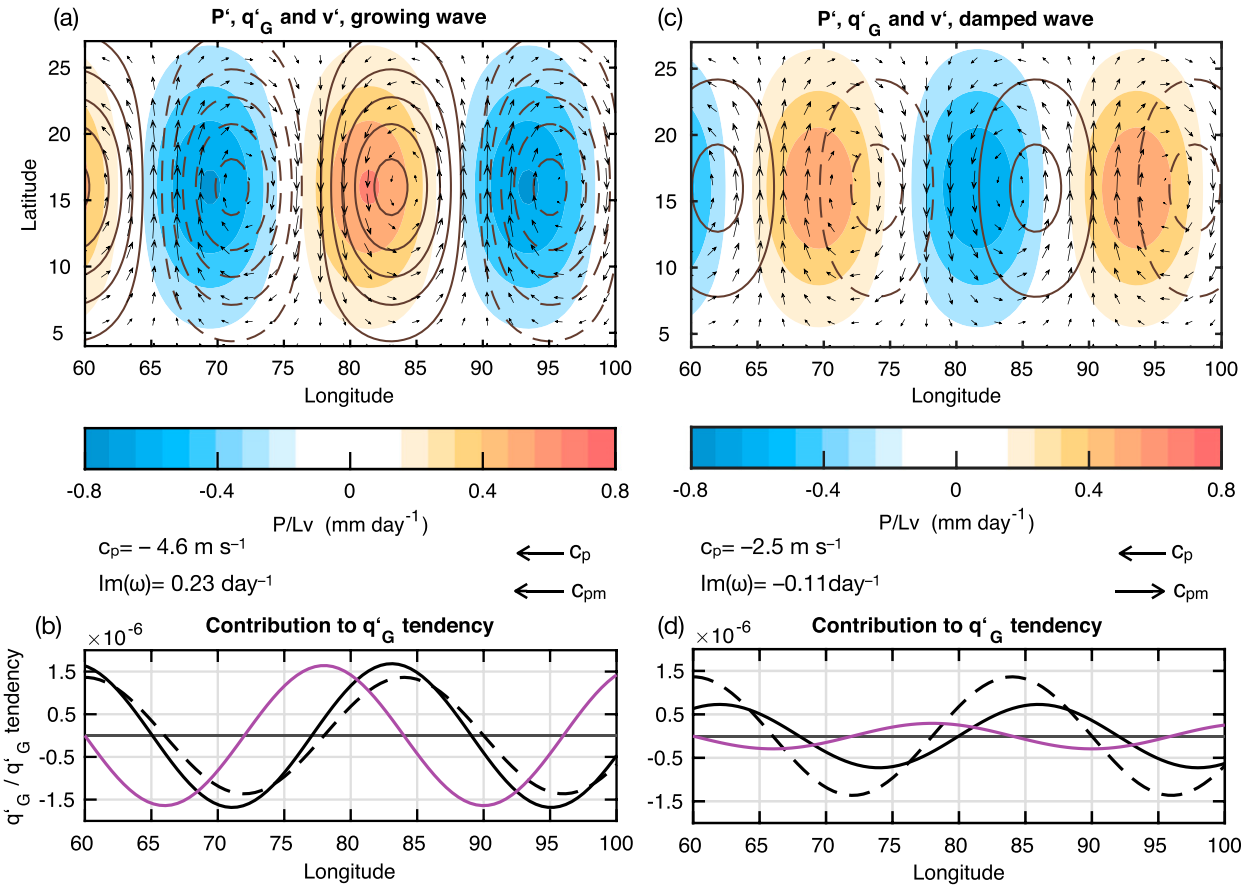

FIG. 10. As in Fig. 7, but showing (a),(c) q'_G as the contoured field; (b),(d) q'_G is shown in solid, the advection of mean q_G ($v'\beta_G$) is shown in purple, and $q'_d/2.5$ is shown as a dashed line. The q'_d and q'_G are in units of s^{-1}, while $-v'\beta_G$ is in units of s^{-1} day^{-1}.

a. Comparison to baroclinic instability

Previous studies have sought to describe SMDs as a result of moist baroclinic instability (Charney and Stern 1962; Bretherton 1966; de Vries et al. 2010), which relies on the existence of counterpropagating waves for their growth (Sanders 1984; Snyder and Lindzen 1991). In this framework, observed SMDs would exhibit structures that tilt eastward with height. This tilt was not found in observations (Cohen and Boos 2016), suggesting that SMDs are not the result of moist baroclinic instability. Unlike existing models of moist baroclinic instability [de Vries et al. 2010; see review by Cohen and Boos (2016)], the framework presented here only involves dry and moist waves in the lower troposphere propagating in the same direction. The middle and upper troposphere do not play a role in the proposed instability. Furthermore, the vertical structure of the idealized SMDs exhibit no tilt, which is more consistent with observations (Cohen and Boos 2016).

Most studies that involve the use of baroclinic instability diagnose convection from the QG omega equation. In the QG framework, ascent occurs in regions of warm-air advection, $P' \propto v'\beta_T$. Using this parameterization, where moisture is not prognostic, yields solutions similar to those shown in section 2, but they are neutrally stable.

In the framework presented here, convection is parameterized in terms of column water vapor. By doing this, isentropic ascent is not just associated with convection but to a positive moisture tendency, as seen in Eq. (15b) and Fig. 10. Such a relationship was found by Adames and Ming (2018), suggesting that moisture may play a critical role in the growth of SMDs.

b. Comparison to the balanced moisture waves of Sobel et al. (2001)

While the framework presented here differs significantly from models of moist baroclinic instability, it resembles the balanced moisture waves described by Sobel et al. [2001; see their Eqs. (42) and (45)]. The main difference between the solutions shown here and theirs

is the presence of a temperature gradient in addition to a meridional moisture gradient and that temperature tendencies are not neglected. This implies that the low-frequency background is not in weak temperature gradient balance. This deviation arises from the land–sea contrast over the South Asian monsoon region and the finite value of the Rossby radius of deformation. We can obtain solutions similar to those of Sobel et al. (2001) by applying the weak temperature gradient (WTG) approximation to Eq. (20). Thus, the balanced moisture waves of Sobel et al. (2001) are a special case of the SMDs described here. Furthermore, the gross PV equation [Eq. (18)] is consistent with the discussion of Sobel (2002), who likened the moisture field to the potential vorticity field in the deep tropics. The idealized SMD solutions are also similar to the moist Rossby waves described by Monteiro and Sukhatme (2016), who looked at the effects of moisture on midlatitude Rossby waves. Our results differ from theirs only because we investigate the case when both temperature and moisture increase with latitude, as observed in the South Asian monsoon.

c. Comparison with moisture mode theory of the MJO

It is worth comparing the moist waves described here to the linear moisture mode theory of the MJO (Fuchs and Raymond 2005, 2007, 2017; Sobel and Maloney 2012, 2013; Adames and Kim 2016). In the moisture mode framework, the growth rate is negatively related to the NGMS and inversely proportional to τ_c. In the approximate solutions shown in section 3 [Eq. (24)], the relationships between NGMS, τ_c, and growth are inverse to those in MJO moisture mode theory. This difference is due to the way that moisture interacts with the anomalies in both frameworks. In idealized SMDs, propagation and growth are partly due to the impact of moisture–convection feedbacks on the vorticity (wind) field. In the MJO, propagation is due to the modulation of moisture by the wind anomalies.

This result implies that the existence of a prognostic moisture equation can cause instability through different mechanisms. In the MJO, the process has been referred to as moisture mode instability or simply moisture instability. The instability for the idealized SMDs may be interpreted as a different type of moisture instability but related to the impact moisture has on PV. Thus, it may be more appropriate to refer to this instability as ''moisture vortex'' instability. That the interaction between moisture and the large-scale flow can lead to more than one instability is interesting, and their manifestation in observations is worth exploring in the future.

d. Radiative heating

Adames and Ming (2018) found that longwave radiative heating plays an important role in the maintenance of the precipitation anomalies in SMDs. While the role of radiative heating was not explicitly included in this study, it can be shown that, to first order, it acts to reduce the NGMS. We can include anomalous radiative heating R in our framework and parameterize it in terms of anomalous precipitation as $R' = -rP'$, where r is the greenhouse enhancement factor (Kim et al. 2015). With this parameterization, P' can be substituted by $P'(1 + r)$ in Eq. (7c). By following the same procedure of section 2, it can be shown that the gross PV is defined as follows:

$$q'_G = \tilde{M}_{\text{eff}} q'_d + (1 - \tilde{M}_{\text{eff}}) q'_m , \tag{29}$$

where $\tilde{M}_{\text{eff}} = \tilde{M}(1 + r) - r$ is the effective gross moist stability. The wave solutions in sections 3–5 are identical, except $\tilde{M}$ is replaced by $\tilde{M}_{\text{eff}}$. A smaller GMS would induce faster growth, as well as selecting slightly smaller scales, as shown in section d of the appendix.

e. Relevance to other tropical depression disturbances

The dispersion relation in Eq. (20) may shed some insight onto other synoptic-scale tropical disturbances. For example, Kiladis et al. (2006) found that divergence of the Q vectors (which is related to β_T) leads convection by 1/8 cycle. Furthermore, Rydbeck and Maloney (2015) and Rydbeck et al. (2017) analyzed easterly waves occurring over the tropical northeastern Pacific, while Hsieh and Cook (2005, 2007) analyzed easterly waves occurring over Africa. The former found that when the waves are developing, meridional moisture advection and vortex stretching play a key role in the growth and propagation of these waves. The latter found that the position of the ITCZ and latent heat release from convection was more important for African easterly development than for the strength of the African easterly jet. Furthermore, Cornforth et al. (2009) found that including moist processes in easterly waves caused their amplitude to triple when compared to dry easterly waves. Supporting these results, a regional modeling study by Berry and Thorncroft (2012) found that African easterly waves weaken steadily when moist convection is turned off in their model (their Fig. 11). They conclude that easterly waves exhibit hybrid adiabatic and diabatic structures. These results suggest that the dynamics of easterly waves over the eastern Pacific and Africa may be described in terms

of a gross potential vorticity, and the waves may grow through moisture vortex instability. It is possible that this instability is also relevant in other regions where disturbances that resemble SMDs form (see Hurley and Boos 2015).

Several studies have suggested that interactions between PV and water vapor play an important role in tropical cyclogenesis (Raymond et al. 2007, 2011). Furthermore, It was found by Bracken and Bosart (2000) that QG ascent may play a role in developing cyclones. By using a convection scheme similar to Betts–Miller, Brammer and Thorncroft (2015) found that developing cyclones exhibit higher positive horizontal moisture advection ahead of the disturbance than nondeveloping ones. Collectively, these results suggest that the framework presented here could be generalized and made applicable to tropical cyclone development.

f. Caveats

There are several caveats to the framework presented here. The mean monsoonal state is characterized by zonal westerlies on the order of 5–10 $\mathrm{m\,s^{-1}}$ and a stronger temperature gradient of 2–4 K $(10^6\,\mathrm{m})^{-1}$, which yields a substantial vertical wind shear. We chose a small temperature gradient that results in a negligible wind shear in order to keep the analysis simple. This results in meridional moisture advection playing a larger role than temperature advection in the idealized SMDs presented here. This is inconsistent with the results of Adames and Ming (2018), who found that temperature advection is the largest contributor to SMD propagation. Because of the weak flow assumed in this study, advection of moisture and vorticity by the background flow do not play a role in the idealized SMDs analyzed here. However, observed mean winds in the tropics have been shown to play a significant role in the propagation of SMDs and other tropical waves (Yanai and Nitta 1967; Lau and Lau 1992; Rydbeck and Maloney 2015). Another caveat is assuming a constant value of τ_c and the NGMS. Large variations in mean moisture precipitation and temperature across the monsoon region can lead to large spatial variations in both the NGMS and τ_c.

Furthermore, the vertical structure of the wave is treated as being directly related to the profile of vertical motion. As a result, the idealized SMDs have a first baroclinic vertical structure. Observed SMDs, however, exhibit a vertical structure where the maximum winds are strongest near the surface. Wang and Xie (1996) interpreted this structure as a combination of barotropic and baroclinic modes in the presence of easterly shear. A more realistic SMD structure could be obtained by having a more realistic mean state with strong easterly shear. While we hypothesize that the instability proposed here is still valid for a more realistic mean state, the simplifications done here to more clearly elucidate our proposed moisture vortex instability is a caveat of this study.

7. Concluding remarks

The linear framework in this study suggests an instability mechanism for tropical lows in a troposphere characterized by high humidity and horizontal moisture and temperature gradients. The proposed instability implies that SMDs may grow without barotropic or baroclinic instabilities. It could also complement these instabilities in regions where they have been shown to be relevant, such as in African easterly waves (Yanai and Nitta 1967; Hall et al. 2006; Hsieh and Cook 2007). It would be interesting to see if such a mechanism can be clearly identified in observations.

The gross PV (q_G) equation presented could be a useful tool in understanding the propagation and growth of tropical disturbances. By just inspecting the magnitude and phase of horizontal advection of q_G with respect to the q_G center, it can be determined whether the disturbance is growing and its propagation speed and direction. A generalized version of Eq. (18a) may be obtained that could be used in diagnostic studies of tropical waves. It would be interesting to see if a generalized form of the gross PV equation can explain the meridional propagation of monsoon depressions by incorporating interactions between moisture and nonlinear horizontal vorticity advection. It was found by Boos et al. (2015) that this ''beta drift'' plays a central role in the northwestward propagation of monsoon low pressure systems.

The linear framework presented here presents an intriguing interpretation of SMDs, which can be tested in model simulations. For example, simulations in which moisture is treated diagnostically may produce weaker disturbances than those that treat moisture prognostically, as suggested by the growth rate in Eq. (24). These and other studies are interesting directions for future study.

Acknowledgments. This work was supported by the National Oceanic and Atmospheric Administration (NOAA) Grant NA15OAR4310099. We thank Eric Maloney for conversations that motivated some of the discussion presented here. We would also like to thank Kuniaki Inoue, Nadir Jeevanjee, Isaac Held, George Kiladis, David Raymond, and an anonymous reviewer for comments that greatly helped improve the contents of the manuscript.

APPENDIX

Derivation and Scaling of the Linear Equations

a. Scaling of the basic equations

The equations shown in Eq. (7) are obtained as a result of a scale analysis of the basic equations on an equatorial beta plane. The equations for horizontal momentum, hydrostatic vertical momentum, mass conservation, and thermodynamic and moisture conservation are written in isobaric coordinates as

$$\frac{\partial U}{\partial t} = -\mathbf{V}\cdot\nabla U - \omega\frac{\partial U}{\partial p} + fV - \frac{\partial \Phi}{\partial x}, \tag{A1a}$$

$$\frac{\partial V}{\partial t} = -\mathbf{V}\cdot\nabla V - \omega\frac{\partial V}{\partial p} - fU - \frac{\partial \Phi}{\partial y}, \tag{A1b}$$

$$\frac{\partial \Phi}{\partial p} = -\frac{R_d T}{p}, \tag{A1c}$$

$$\nabla\cdot\mathbf{V} = -\frac{\partial \omega}{\partial p}, \tag{A1d}$$

$$C_p\frac{\partial T}{\partial t} = -C_p\mathbf{V}\cdot\nabla T - \omega\frac{\partial s}{\partial p} + Q_1, \tag{A1e}$$

$$\frac{\partial q}{\partial t} = -\mathbf{V}\cdot\nabla q - \omega\frac{\partial q}{\partial p} + Q_2, \tag{A1f}$$

where U and V are the zonal and meridional winds, respectively; Φ is the geopotential; ω is the vertical velocity; $s = C_pT + \Phi$ is the dry static energy; Q_1 is the apparent heat source; and Q_2 is the apparent moisture source, following the notation of Yanai et al. (1973). In this model, we will assume that diabatic heating is due to phase changes in water vapor, so $Q_1 = -Q_2 = Q$. The column integral of Q is the surface precipitation rate $\langle Q\rangle = P$, where P is expressed in units of $\mathrm{W\,m^{-2}}$. Note that we do not include radiative heating or surface fluxes in this model. We have used uppercase letters for U, V, and Φ to differentiate the horizontal wind and geopotential fields from their vertically truncated counterparts. We have assumed that the equations satisfy hydrostatic balance and that the flow is approximately incompressible.

The fields in Eq. (A1) are then linearized with respect to a zonally symmetric mean state where mean moisture and temperature increase with latitude, qualitatively consistent with the with the South Asian monsoon:

$$\mathbf{V} = \overline{\mathbf{V}} + \mathbf{V}', \tag{A2a}$$

$$\omega = \overline{\omega} + \omega', \tag{A2b}$$

$$\Phi = \overline{\Phi} + \Phi', \tag{A2c}$$

$$T = \overline{T} + T', \tag{A2d}$$

$$q = \overline{q} + q', \tag{A2e}$$

$$Q = \overline{Q} + Q'. \tag{A2f}$$

To keep the analysis simple, the mean and anomalous flow are assumed to be on the order of $1\,\mathrm{m\,s^{-1}}$. All other variables are scaled so that they are consistent with these winds.

For a wind field U on the order of $1\,\mathrm{m\,s^{-1}}$, a planetary vorticity of $f_0 = 4\times10^{-5}\,\mathrm{s^{-1}}$, and a horizontal-scale L on the order of $10^6\,\mathrm{m}$, the mean zonal flow is, to first order, in geostrophic balance. It can be shown that this scaling is consistent with a Rossby number on the order of $\sim10^{-1}$ [$\mathrm{Ro} = U/(f_0L)$]. It follows that the thermal wind U_T is on the order of $1\,\mathrm{m\,s^{-1}}$ for a horizontal temperature change on the order of $10^{-1}\,\mathrm{K}\,(10^6\,\mathrm{m})^{-1}$.

Following Sobel et al. (2001), we can estimate the magnitude of the vertical velocity from the magnitude of the heating. We assume that Q is on the same order of magnitude as the vertical dry static energy advection. It will further be assumed that $\overline{Q} \gg Q'$ so that $\overline{Q}$ is on the order of $10^{-2}\,\mathrm{J\,kg^{-1}\,s^{-1}}$ and Q' an order of magnitude smaller. It follows that $\overline{P}$ is on the order of $10^2\,\mathrm{W\,m^{-2}}$. This implies a climatological-mean rainfall rate on the order of $10\,\mathrm{mm\,day^{-1}}$ and a perturbation of $1\,\mathrm{mm\,day^{-1}}$;

$$\overline{W}\frac{\delta\overline{S}}{\delta p} \sim \overline{Q}, \tag{A3a}$$

$$W'\frac{\delta\overline{S}}{\delta p} \sim Q'. \tag{A3b}$$

If the vertical change in mean dry static energy is on the order of $10^4\,\mathrm{J\,kg^{-1}}$, then $\overline{W}\sim 10^{-1}\,\mathrm{Pa\,s^{-1}}$ and $W' \sim 10^{-2}\,\mathrm{Pa\,s^{-1}}$, respectively. It can be shown that the anomalies in DSE are much smaller than its mean value so that the nonlinear vertical DSE advection term contributes little to the thermodynamic balance.

From the scaling in Eq. (A3a), we can verify that the mean state follows the scaling $\overline{W}\sim V\delta p/L$. However, for the pertubation fields, $W' \ll V\delta p/L$, which indicates that the anomaly fields are approximately nondivergent;

$$D' \ll \zeta', \tag{A4}$$

which is consistent with the slowly propagating linear solutions of Sobel et al. (2001) and the scale analysis of Yano and Bonazzola (2009). For the parameters used here, $\zeta' \sim 10^{-6}\,\mathrm{s^{-1}}$ and $D' \sim 10^{-7}\,\mathrm{s^{-1}}$. This can further be verified by defining a Rossby number for wave motion $\mathrm{Ro} = 1/(\delta t f_0)$, as in Raymond et al. (2015). For a 5-day wave at 16°N, this yields $\mathrm{Ro} = 0.06$, although the scaling arguments used here suggest that the value

could be as high as 0.25. Though we have verified that the wave solutions in section 3 are approximately nondivergent, faster waves may not be so, a caveat of this study.

The moisture equation [Eq. (A1f)] is scaled as follows. Because vertical variations in moisture are much larger than horizontal variations, two different scales are used for them ($\delta_p q$ and $\delta_L q$). In the tropics, where water vapor concentrations are high, vertical variations in mean latent heat are comparable to those in mean dry static energy, such that $\delta_p \overline{q} \sim \delta \overline{S}$. Horizontal variations in column wapor in the tropics are often on the order of 5–10 mm, which implies that $\delta_L q \sim 10^3\,\mathrm{J\,m^2}$.

We can verify the consistency of the scaling above by expanding Eq. (4) into a Taylor series and truncating on the second term, where the first term corresponds to $\overline{P}$ and the second term to P':

$$P(\mathrm{RH}) \simeq \overline{P}(\overline{\mathrm{RH}}) + \mathrm{RH}' \frac{\partial P}{\partial \mathrm{RH}}\bigg|_{\overline{\mathrm{RH}}}, \tag{A5}$$

where RH is also expanded into a Taylor series:

$$\mathrm{RH} \simeq \overline{\mathrm{RH}} + \frac{\langle q' \rangle - \overline{\mathrm{RH}} \langle q_s' \rangle}{\langle \overline{q}_s \rangle}; \tag{A6}$$

based on a temperature anomaly on the order of 10^{-1}, we can show that the perturbations in $\langle q_s' \rangle$ are small, which leads to

$$\mathrm{RH}' \simeq \langle q' \rangle / \langle \overline{q}_s \rangle; \tag{A7}$$

after applying these approximations, Eq. (5) can be obtained. Through scaling of Eq. (5), it can be shown that $P' \ll \overline{P}$ for values of $\langle q' \rangle$ of $\sim 10^0 L_v$ of $\sim 10^0 L_v\ \mathrm{J\,m^{-2}}$ since $a \sim 10^2$ and $\langle \overline{q}_s \rangle \sim 10^2 L_v\ \mathrm{J\,m^{-2}}$. Thus, column water vapor perturbations are much smaller, by nearly two orders of magnitude, than the mean water vapor field.

With the scaling arguments discussed above, which are summarized in in Table A1, the linearized momentum, thermodynamic, and moisture equations take the following form:

$$\frac{\partial u'}{\partial t} = f v' - \frac{\partial \phi'}{\partial x}, \tag{A8a}$$

$$\frac{\partial v'}{\partial t} = -f u' - \frac{\partial \phi'}{\partial y}, \tag{A8b}$$

$$\frac{\partial T'}{\partial t} = -v' \frac{\partial \overline{T}}{\partial y} - \frac{\omega'}{C_p} \frac{\partial \overline{s}}{\partial p} + \frac{Q'}{C_p}, \tag{A8c}$$

$$\frac{\partial q'}{\partial t} = -v' \frac{\partial \overline{q}}{\partial y} - \omega' \frac{\partial \overline{q}}{\partial p} - Q'. \tag{A8d}$$

TABLE A1. Values used in the scaling of the basic equations in section a of the appendix.

Scaling variable	Symbol	Value and units
Horizontal scale	L	10^6 m
Vertical scale	δp	10^5 Pa
Wave time scale	δt	10^5 s
Mean and anomalous horizontal winds	U	$10^0\,\mathrm{m\,s^{-1}}$
Thermal wind scale	U_T	$10^0\,\mathrm{m\,s^{-1}}$
Rossby number	Ro	10^{-1}
Mean vertical velocity	$\overline{W}$	$10^{-1}\,\mathrm{Pa\,s^{-1}}$
Anomalous vertical velocity	W'	$10^{-2}\,\mathrm{Pa\,s^{-1}}$
Mean and anomalous geopotential	Φ	$10^1\,\mathrm{m^2\,s^{-2}}$
Mean and anomalous temperature scale	T	10^{-1} K
Anomalous latent heat	q'	$10^2\,\mathrm{J\,m^2}$
Mean heating from condensation	$\overline{Q}$	$10^{-2}\,\mathrm{J\,kg^{-1}\,s^{-1}}$
Anomalous heating from condensation	Q'	$10^{-3}\,\mathrm{J\,kg^{-1}\,s^{-1}}$
Vertical change in mean dry static energy	$\delta_p \overline{s}$	$10^4\,\mathrm{J\,kg^{-1}}$
Mean vertical latent heat scale	$\delta_P \overline{q}$	$10^4\,\mathrm{J\,m^2}$
Mean horizontal latent heat scale	$\delta_L \overline{q}$	$10^3\,\mathrm{J\,m^2}$

Note that the term corresponding to the advection of mean temperature by the anomalous meridional winds was not neglected. While this term is negligibly small in the thermodynamic equation, it has a significant contribution to the propagation of the moist waves discussed here. The scale analysis performed here suggests that β_T is on the order of $10^{-12}\,\mathrm{m^{-1}\,s^{-1}}$, an order of magnitude smaller than β. This value of β_T is nonnegligible in the gross PV equation [Eq. (18a)] when the normalized gross moist stability $\tilde{M}$ is small. This can be shown by scaling β_G in Eq. (18a), which yields

$$\tilde{M}\beta \sim (1 - \tilde{M})\beta_T. \tag{A9}$$

In this case, a small amount of temperature advection can induce precipitation, whose vortex stretching is comparable to that of advection of planetary vorticity by the mean winds. Meridional advection of mean moisture by the anomalous winds follows a similar scaling.

b. *Vertical truncation of the equations*

In this section, we describe the vertical truncation of the equations shown in section 2. Following Neelin and Zeng (2000), we separate the vertical velocity field into a horizontal divergence field D and a structure function Ω that describes the profile of vertical velocity

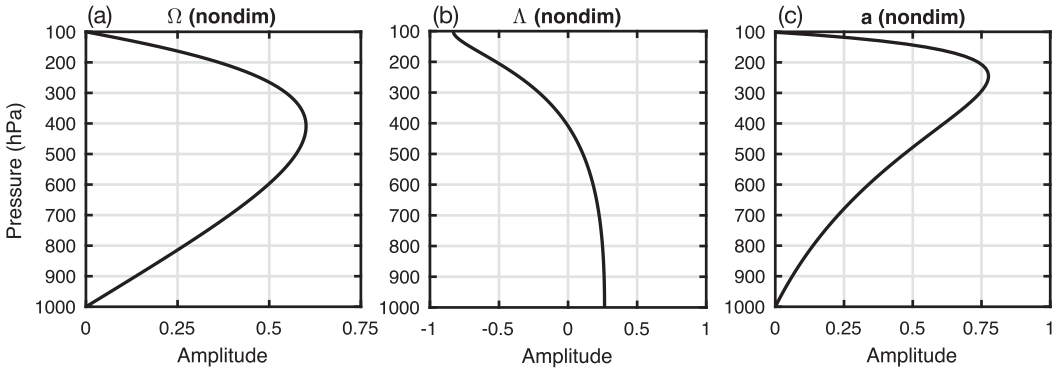

FIG. A1. Basis functions of (a) vertical velocity Ω, (b) horizontal winds and geopotential Λ, and (c) temperature a. The Ω has been normalized by dividing by $\hat{p}$.

ω (note that in section 3, ω corresponds to the wave frequency instead):

$$\omega'(x,y,p,t) = D'(x,y,t)\Omega(p), \tag{A10}$$

where we make use of a single vertical structure function that corresponds to deep convection (a first baroclinic mode in vertical motion). Following a rigid lid boundary condition, Ω must be equal to zero at 1000 and 100 hPa. We use a simple formula for Ω that satisfies these conditions, which is similar to the formulas used by Haertel et al. (2008) and Kiladis et al. (2009):

$$\Omega(p) \simeq \hat{p}(p/p_s)^{1/2}\sin[m\ln(p_s/p)], \tag{A11}$$

where $\hat{p} \simeq 200$ hPa is a reference pressure, $p_s = 1000$ hPa is the surface pressure, and $m = \pi/\ln(p_s/p_t)$ is the vertical wavenumber. The vertical profile of Ω is shown in Fig. A1. Although similar, this profile is slightly different from the one used by Adames and Kim (2016).

Similarly, the anomalous horizontal winds $\mathbf{V}' = (U', V')$, the geopotential Φ', and the temperature T' are separated into a horizontal component and a vertical structure function:

$$\mathbf{V}'(x,y,p,t) = \mathbf{v}'(x,y,t)\Lambda(p), \tag{A12a}$$
$$\Phi'(x,y,p,t) = \phi'(x,y,t)\Lambda(p), \tag{A12b}$$
$$T'(x,y,p,t) = \tau'(x,y,t)a(p), \tag{A12c}$$

where $\mathbf{v} = (u, v)$ and the structure function Λ is obtained from Ω through mass continuity:

$$\Lambda(p) = -\frac{\partial\Omega(p)}{\partial p} \tag{A13}$$

and a is obtained from hydrostatic balance:

$$a(p) = \frac{\partial\Lambda(p)}{\partial\ln p}. \tag{A14}$$

The vertical profiles of Λ and a are shown in Figs. A1b and A1c, respectively. Through this truncation, we can verify that

$$\phi' = -R_d\boldsymbol{\tau}', \tag{A15a}$$
$$D' = \nabla\cdot\mathbf{v}', \tag{A15b}$$

and we can obtain the equations shown in Eq. (7). Truncation of the moisture field is discussed in the following section.

c. Mean state

In this section, we present the calculation of values for the mean-state fields. The mean temperature field can be separated into a leading-order profile with a lapse rate that is constant with height and a second-order term that accounts for meridional variations in temperature:

$$\overline{T}(y,p) = \overline{T}_0(p) + y\delta T(p), \tag{A16}$$

where

$$\overline{T}_0 = \overline{T}_s\left(\frac{p}{p_s}\right)^{R_{d\gamma}/g}, \tag{A17}$$

where $\overline{T}_s = 302$ K is the surface temperature and $\gamma = 7.0\,\mathrm{K\,km^{-1}}$ is the environmental lapse rate. For simplicity, the meridional gradient term is written as $\delta T = T_c\Lambda$, where $T_c = 2$ K. Using this simple profile yields a simple meridional gradient in $\overline{T}$ that is consistent with the scaling from the previous section, and a value of $\beta_T = 2.5\times10^{-12}\,\mathrm{m^{-1}\,s^{-1}}$ is obtained.

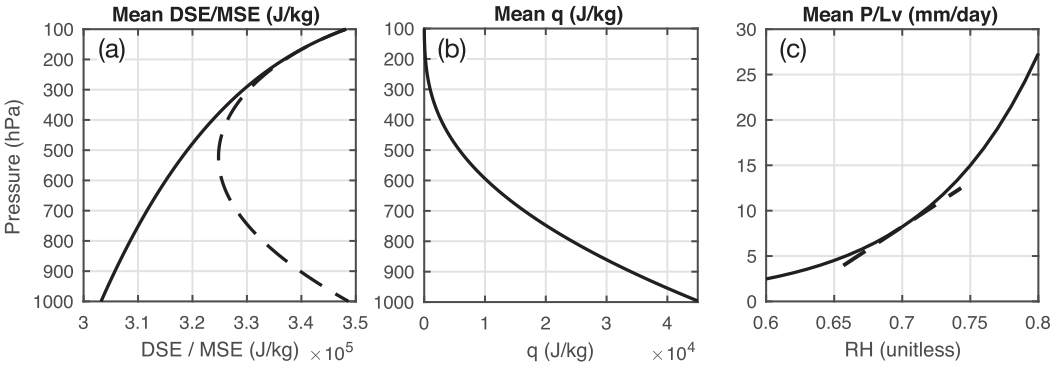

FIG. A2. Vertical profiles of (a) mean dry static energy $\overline{s}$ (solid) and moist static energy (dashed), and (b) latent energy $\overline{q}$. (c) Mean precipitation $\overline{P}$ as a function of mean column relative humidity $\overline{\mathrm{RH}}$. Dashed line corresponds to approximate relation using Eq. (A5) with a reference RH of 0.70.

We can obtain a profile of $\overline{\Phi}$ that is consistent with $\overline{T}$ through the hydrostatic equation:

$$\overline{\Phi}(p) \simeq \frac{g\overline{T_s}}{\gamma}\left[1-\left(\frac{p}{p_s}\right)^{R_d\gamma/g}\right]; \tag{A18}$$

note that this is an approximate profile for the geopotential field. As discussed in the previous section, the mean flow is characterized by a zonal wind on the order of $1\,\mathrm{m\,s^{-1}}$. Meridional variations in $\overline{\Phi}$ exist in order to satisfy geostrophic balance with this wind. However, they are not discussed here since they are small and are not of primary importance to Eq. (7). The mean dry static energy $\overline{s}$ can be obtained from $\overline{T}$ and $\overline{\Phi}$, and its vertical profile is shown in Fig. A2a.

The moist variables are chosen to be consistent with the saturation specific humidity, which is obtained from the following formula (Wallace and Hobbs 2006):

$$\overline{q}_s = \frac{0.622e_s}{0.01p - 0.378e_s}, \tag{A19a}$$

$$e_s \simeq 6.11\exp\left[5420\left(\frac{1}{273}-\frac{1}{\overline{T}}\right)\right], \tag{A19b}$$

where e_s is the saturation vapor pressure. For the mean temperature profile discussed above, we obtain a column-integrated value of $\langle\overline{q}_s\rangle = 70\,L_v$ mm. Because meridional variations in $\overline{T}$ are small, meridional variations in $\langle\overline{q}_s\rangle$ are much smaller than its mean value at 16°N, on the order of 1–2 mm, and thus, a constant value at the reference latitude can be used. This approximation is adequate for the linearized equation for P', but it is much less accurate for Eq. (4).

We can write the mean specific humidity as a function of q_s scaled by a constant column relative humidity:

$$\overline{q} = \overline{\mathrm{RH}} \times \overline{q}_s. \tag{A20}$$

If $\overline{\mathrm{RH}} = 0.72$, we find that $\langle\overline{q}\rangle = 49L_v$ mm, $a = 12$, and $P_0 = 1.8\times10^{-3}\times L_v\ \mathrm{mm\,day^{-1}}$. We obtain that $\overline{P} = 8.2\,L_v\,\mathrm{mm\,day^{-1}}$ and $\tau_c = 12.2$ h. Note that the value of P_0 differs from those of Bretherton et al. (2004), but it is used in order to be consistent with the scaling in section a of the appendix. For reference, the vertical structure of $\overline{q}$ and $\overline{P}$ as a function of RH are shown in Figs. A2b and A2c, respectively.

d. *Propagation and growth for various parameter values*

In section 3, we obtained linear wave solutions that could describe monsoon low pressure systems. The solutions were shown for specific parameter values. In this section, we analyze how changing these parameter values affects these solutions. Figure A3a shows the real component of the wave frequency, as obtained from Eq. (20) for $l = 0$ and various values of β_q. Frequency is a maximum near zonal wavenumber 6, and frequency increases as β_q increases. Figure A3b shows the wave frequency for different values of τ_c. It is clear that larger values of τ_c result in weaker propagation. This is due to a longer delay in convective onset, which results in precipitation contributing less to the vorticity tendency, as shown in section 4. When variation in NGMS are considered (Fig. A3c), we see a shift of the maximum frequency toward smaller k as the NGMS increases. Between zonal wavenumbers 10 and 40, we observe a decrease in frequency as NGMS increases, likely from a decreasing contribution of moist

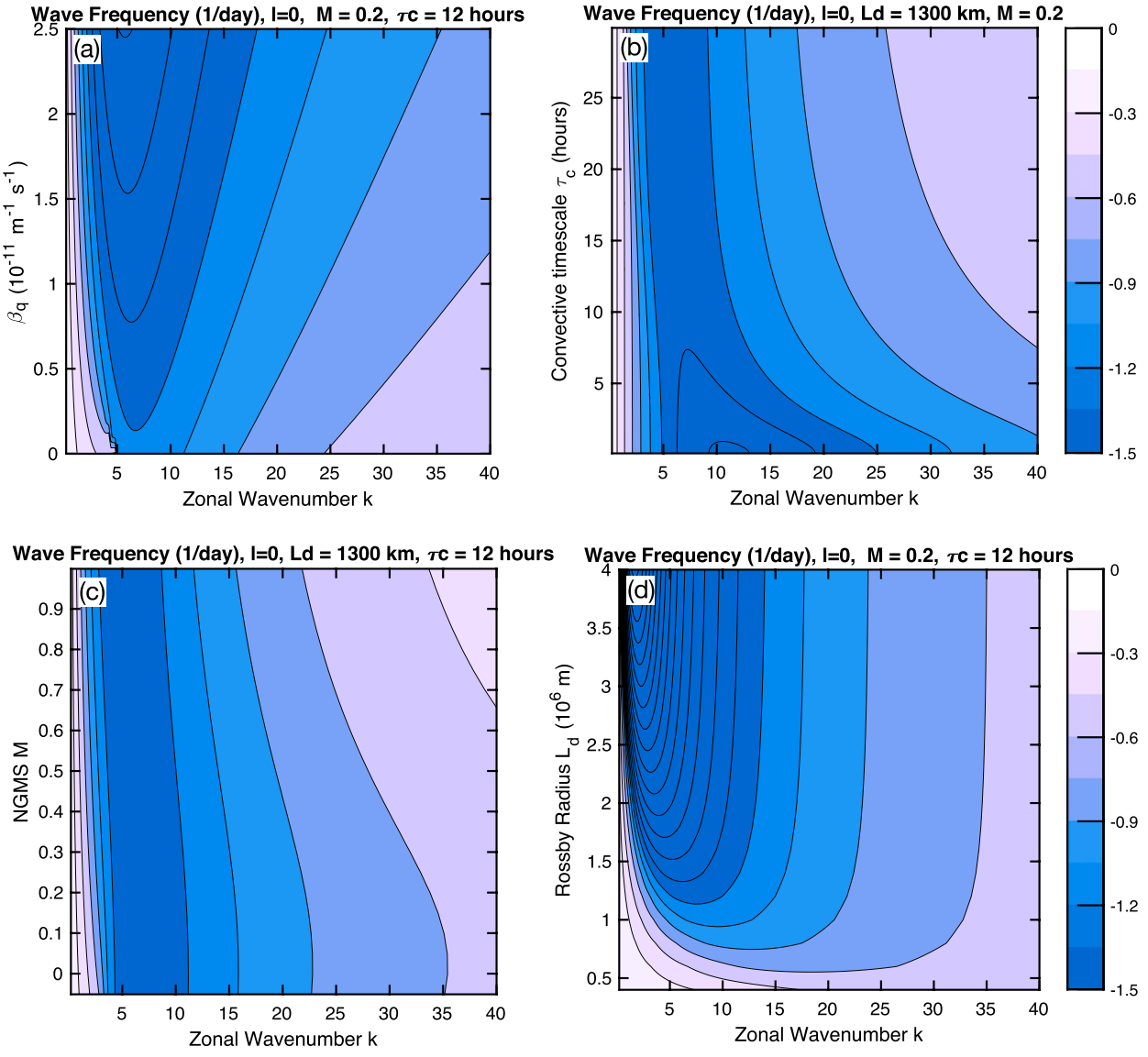

FIG. A3. (a) Real component of the dispersion relation in Eq. (20) for $l = 0$ and various values of β_q. (b) As in (a), but as a function of zonal wavenumber and τ_c. (c) Frequency as a function of k and NGMS. (d) Frequency as a function of k and L_d. Values of other parameters are shown above each panel.

processes to propagation. Increasing the Rossby radius of deformation, shown in Fig. A3d, yields faster propagation across all wavenumbers.

Figure A4a shows the growth rate of the dispersion shown in Eq. (20) for $l = 0$ and various values of β_q. Stronger growth is observed for larger values of β_q, and the maximum growth shifts to smaller k as β_q increases. Damping at the largest scales weakens as β_q increases. The growth rate for $l = 0$ but for various values of τ_c is shown in Fig. A4b. The strongest growth occurs for time scales of 4–6 h and near zonal wavenumber 15. For larger values of τ_c, growth is weaker and is shifted toward smaller scales, with the strongest growth occurring near zonal wavenumber 20 for τ_c values of 1 day. For variations in the NGMS ($\tilde{M}$), shown in Fig. A4c, we find that growth is stronger for smaller values of NGMS and the maximum growth occurs at smaller scales, consistent with Eqs. (24) and (28). As the NGMS increases, growth occurs at larger scales, shifting from zonal wavenumber 20 for NGMS of ~0. While the approximate solutions are singular near $\tilde{M} \to 0$, the dispersion in Eq. (20) is not, and Fig. A4b reveals that growth increases as $\tilde{M}$ becomes negative. The growth rate as a function of the Rossby radius of deformation L_d is shown in Fig. A4d.

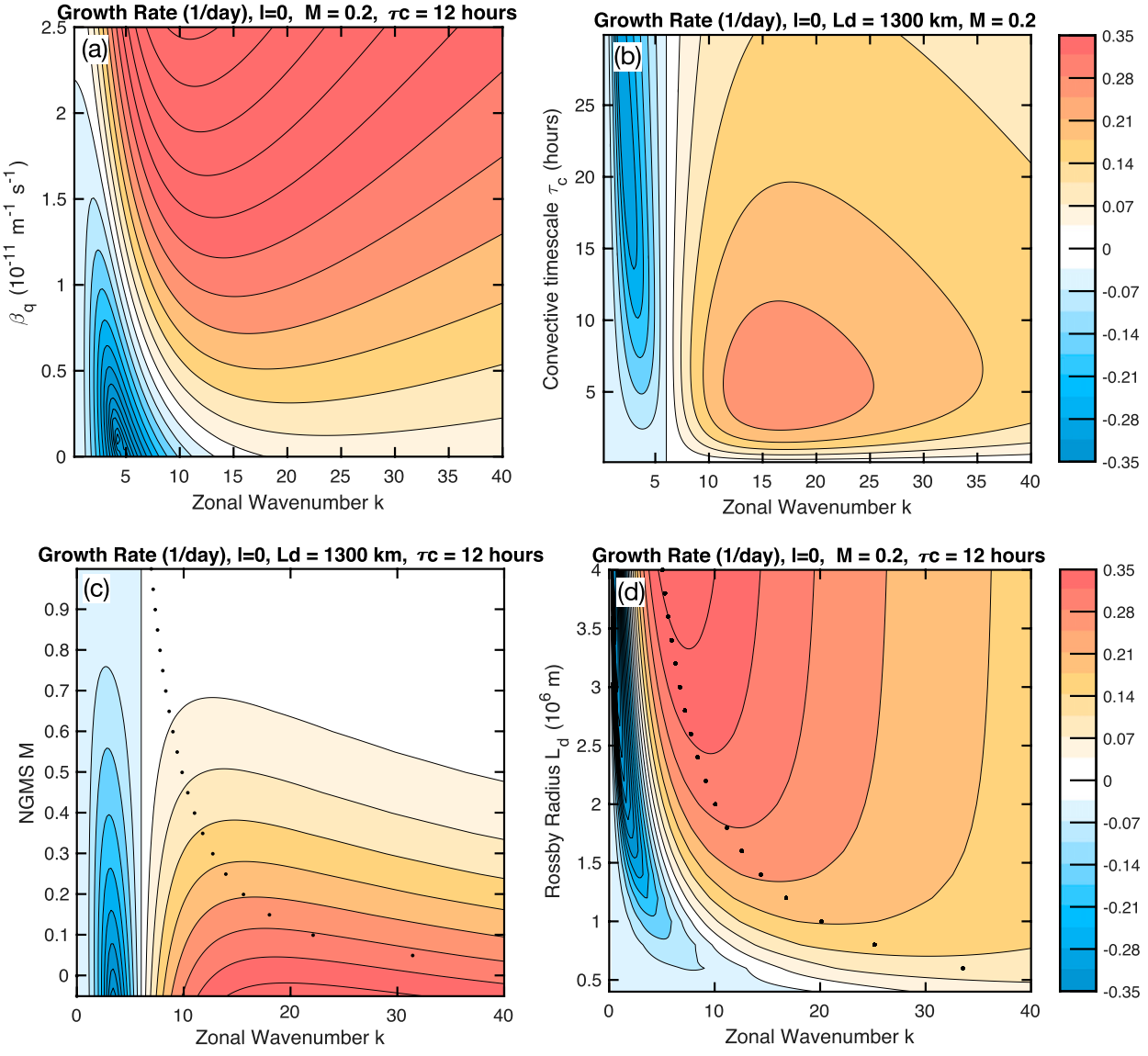

FIG. A4. As in Fig. A3, but showing the growth rate. (c),(d) Dots show the zonal scale estimated from Eq. (28), which roughly corresponds to the maximum growth rate in the approximate solution (Eq. 24).

As L_d increases, growth becomes stronger and shifts toward the larger scales, consistent with Eq. (28). When L_d is small, the solution becomes weakly damped at nearly all wavenumbers.

REFERENCES

Adames, Á. F., 2017: Precipitation budget of the Madden–Julian oscillation. *J. Atmos. Sci.*, **74**, 1799–1817, https://doi.org/10.1175/JAS-D-16-0242.1.

——, and D. Kim, 2016: The MJO as a dispersive, convectively coupled moisture wave: Theory and observations. *J. Atmos. Sci.*, **73**, 913–941, https://doi.org/10.1175/JAS-D-15-0170.1.

——, and Y. Ming, 2018: Moisture and moist static energy budgets of South Asian monsoon low pressure systems in GFDL AM4.0. *J. Atmos. Sci.*, https://doi.org/10.1175/JAS-D-17-0309.1, in press.

Aravequia, J. A., V. B. Rao, and J. P. Bonatti, 1995: The role of moist baroclinic instability in the growth and structure of monsoon depressions. *J. Atmos. Sci.*, **52**, 4393–4409, https://doi.org/10.1175/1520-0469(1995)052<4393:TROMBI>2.0.CO;2.

Berry, G. J., and C. D. Thorncroft, 2012: African easterly wave dynamics in a mesoscale numerical model: The upscale role of convection. *J. Atmos. Sci.*, **69**, 1267–1283, https://doi.org/10.1175/JAS-D-11-099.1.

Betts, A. K., 1986: A new convective adjustment scheme. Part I: Observational and theoretical basis. *Quart. J. Roy. Meteor. Soc.*, **112**, 677–691, https://doi.org/10.1002/qj.49711247307.

——, and M. J. Miller, 1986: A new convective adjustment scheme. Part II: Single column tests using GATE wave, BOMEX,

ATEX and Arctic air-mass data sets. *Quart. J. Roy. Meteor. Soc.*, **112**, 693–709, https://doi.org/10.1002/qj.49711247308.

Boos, W. R., J. V. Hurley, and V. S. Murthy, 2015: Adiabatic westward drift of Indian monsoon depressions. *Quart. J. Roy. Meteor. Soc.*, **141**, 1035–1048, https://doi.org/10.1002/qj.2454.

Bracken, W. E., and L. F. Bosart, 2000: The role of synoptic-scale flow during tropical cyclogenesis over the North Atlantic Ocean. *Mon. Wea. Rev.*, **128**, 353–376, https://doi.org/10.1175/1520-0493(2000)128<0353:TROSSF>2.0.CO;2.

Brammer, A., and C. D. Thorncroft, 2015: Variability and evolution of African easterly wave structures and their relationship with tropical cyclogenesis over the eastern Atlantic. *Mon. Wea. Rev.*, **143**, 4975–4995, https://doi.org/10.1175/MWR-D-15-0106.1.

Bretherton, C. S., M. E. Peters, and L. E. Back, 2004: Relationships between water vapor path and precipitation over the tropical oceans. *J. Climate*, **17**, 1517–1528, https://doi.org/10.1175/1520-0442(2004)017<1517:RBWVPA>2.0.CO;2.

Bretherton, F. P., 1966: Baroclinic instability and the short wavelength cut-off in terms of potential vorticity. *Quart. J. Roy. Meteor. Soc.*, **92**, 335–345, https://doi.org/10.1002/qj.49709239303.

Charney, J. G., and M. E. Stern, 1962: On the stability of internal baroclinic jets in a rotating atmosphere. *J. Atmos. Sci.*, **19**, 159–172, https://doi.org/10.1175/1520-0469(1962)019<0159:OTSOIB>2.0.CO;2.

Cohen, N. Y., and W. R. Boos, 2016: Perspectives on moist baroclinic instability: Implications for the growth of monsoon depressions. *J. Atmos. Sci.*, **73**, 1767–1788, https://doi.org/10.1175/JAS-D-15-0254.1.

Cornforth, R. J., B. J. Hoskins, and C. D. Thorncroft, 2009: The impact of moist processes on the African easterly jet–African easterly wave system. *Quart. J. Roy. Meteor. Soc.*, **135**, 894–913, https://doi.org/10.1002/qj.414.

de Vries, H., J. Methven, T. H. A. Frame, and B. J. Hoskins, 2010: Baroclinic waves with parameterized effects of moisture interpreted using Rossby wave components. *J. Atmos. Sci.*, **67**, 2766–2784, https://doi.org/10.1175/2010JAS3410.1.

Ding, Y., and D. R. Sikka, 2006: Synoptic systems and weather. *The Asian Monsoon*, Springer, 131–201, https://doi.org/10.1007/3-540-37722-0_4.

Frierson, D. M. W., 2007: The dynamics of idealized convection schemes and their effect on the zonally averaged tropical circulation. *J. Atmos. Sci.*, **64**, 1959–1976, https://doi.org/10.1175/JAS3935.1.

Fuchs, Ž., and D. J. Raymond, 2005: Large-scale modes in a rotating atmosphere with radiative–convective instability and WISHE. *J. Atmos. Sci.*, **62**, 4084–4094, https://doi.org/10.1175/JAS3582.1.

——, and ——, 2007: A simple, vertically resolved model of tropical disturbances with a humidity closure. *Tellus*, **59A**, 344–354, https://doi.org/10.1111/j.1600-0870.2007.00230.x.

——, and ——, 2017: A simple model of intraseasonal oscillations. *J. Adv. Model. Earth Syst.*, **9**, 1195–1211, https://doi.org/10.1002/2017MS000963.

Godbole, R. V., 1977: The composite structure of the monsoon depression. *Tellus*, **29**, 25–40, https://doi.org/10.3402/tellusa.v29i1.11327.

Haertel, P. T., G. N. Kiladis, A. Denno, and T. M. Rickenbach, 2008: Vertical-mode decompositions of 2-day waves and the Madden–Julian oscillation. *J. Atmos. Sci.*, **65**, 813–833, https://doi.org/10.1175/2007JAS2314.1.

Hall, N. M. J., G. N. Kiladis, and C. D. Thorncroft, 2006: Three-dimensional structure and dynamics of African easterly waves. Part II: Dynamical modes. *J. Atmos. Sci.*, **63**, 2231–2245, https://doi.org/10.1175/JAS3742.1.

Hsieh, J.-S., and K. H. Cook, 2005: Generation of African easterly wave disturbances: Relationship to the African easterly jet. *Mon. Wea. Rev.*, **133**, 1311–1327, https://doi.org/10.1175/MWR2916.1.

——, and ——, 2007: A study of the energetics of African easterly waves using a regional climate model. *J. Atmos. Sci.*, **64**, 421–440, https://doi.org/10.1175/JAS3851.1.

Hunt, K. M. R., and A. G. Turner, 2017: The effect of horizontal resolution on Indian monsoon depressions in the Met Office NWP model. *Quart. J. Roy. Meteor. Soc.*, **143**, 1756–1771, https://doi.org/10.1002/qj.3030.

——, ——, P. M. Inness, D. E. Parker, and R. C. Levine, 2016: On the structure and dynamics of Indian monsoon depressions. *Mon. Wea. Rev.*, **144**, 3391–3416, https://doi.org/10.1175/MWR-D-15-0138.1.

Hurley, J. V., and W. R. Boos, 2015: A global climatology of monsoon low-pressure systems. *Quart. J. Roy. Meteor. Soc.*, **141**, 1049–1064, https://doi.org/10.1002/qj.2447.

Janiga, M. A., and C. D. Thorncroft, 2013: Regional differences in the kinematic and thermodynamic structure of African easterly waves. *Quart. J. Roy. Meteor. Soc.*, **139**, 1598–1614, https://doi.org/10.1002/qj.2047.

Jiang, X., M. Zhao, E. D. Maloney, and D. E. Waliser, 2016: Convective moisture adjustment time scale as a key factor in regulating model amplitude of the Madden-Julian oscillation. *Geophys. Res. Lett.*, **43**, 10 412–10 419, https://doi.org/10.1002/2016GL070898.

Kiladis, G. N., C. D. Thorncroft, and N. M. J. Hall, 2006: Three-dimensional structure and dynamics of African easterly waves. Part I: Observations. *J. Atmos. Sci.*, **63**, 2212–2230, https://doi.org/10.1175/JAS3741.1.

——, M. C. Wheeler, P. T. Haertel, K. H. Straub, and P. E. Roundy, 2009: Convectively coupled equatorial waves. *Rev. Geophys.*, **47**, RG2003, https://doi.org/10.1029/2008RG000266; Corrigendum, **49**, RG3004, https://doi.org/10.1029/2008RG000266.

Kim, D., M.-S. Ahn, I.-S. Kang, and A. D. Del Genio, 2015: Role of longwave cloud–radiation feedback in the simulation of the Madden–Julian oscillation. *J. Climate*, **28**, 6979–6994, https://doi.org/10.1175/JCLI-D-14-00767.1.

Krishnakumar, V., R. N. Keshavamurty, and S. V. Kasture, 1992: Moist baroclinic instability and the growth of monsoon depressions—Linear and nonlinear studies. *Proc. Indian Acad. Sci., Earth Planet. Sci.*, **101**, 123–152.

Krishnamurti, T.-N., M. Kanamitsu, R. Godbole, C.-B. Chang, F. Carr, and J. H. Chow, 1975: Study of a monsoon depression (I): Synoptic structure. *J. Meteor. Soc. Japan*, **53**, 227–239, https://doi.org/10.2151/jmsj1965.53.4_227.

——, ——, ——, ——, ——, and ——, 1976: Study of a monsoon depression (II): Dynamical structure. *J. Meteor. Soc. Japan*, **54**, 208–226, https://doi.org/10.2151/jmsj1965.54.4_208.

Krishnamurti, T. N., A. Martin, R. Krishnamurti, A. Simon, A. Thomas, and V. Kumar, 2013: Impacts of enhanced CCN on the organization of convection and recent reduced counts of monsoon depressions. *Climate Dyn.*, **41**, 117–134, https://doi.org/10.1007/s00382-012-1638-z.

Lau, K.-H., and N.-C. Lau, 1990: Observed structure and propagation characteristics of tropical summertime synoptic scale disturbances. *Mon. Wea. Rev.*, **118**, 1888–1913, https://doi.org/10.1175/1520-0493(1990)118<1888:OSAPCO>2.0.CO;2.

——, and ——, 1992: The energetics and propagation dynamics of tropical summertime synoptic-scale disturbances. *Mon. Wea. Rev.*, **120**, 2523–2539, https://doi.org/10.1175/1520-0493(1992)120<2523:TEAPDO>2.0.CO;2.

Mak, M., 1982: On moist quasi-geostrophic baroclinic instability. *J. Atmos. Sci.*, **39**, 2028–2037, https://doi.org/10.1175/1520-0469(1982)039<2028:OMQGBI>2.0.CO;2.

Monteiro, J. M., and J. Sukhatme, 2016: Quasi-geostrophic dynamics in the presence of moisture gradients. *Quart. J. Roy. Meteor. Soc.*, **142**, 187–195, https://doi.org/10.1002/qj.2644.

Mooley, D. A., 1973: Some aspects of Indian monsoon depressions and the associated rainfall. *Mon. Wea. Rev.*, **101**, 271–280, https://doi.org/10.1175/1520-0493(1973)101<0271:SAOIMD>2.3.CO;2.

Neelin, J. D., and I. M. Held, 1987: Modeling tropical convergence based on the moist static energy budget. *Mon. Wea. Rev.*, **115**, 3–12, https://doi.org/10.1175/1520-0493(1987)115<0003:MTCBOT>2.0.CO;2.

——, and N. Zeng, 2000: A quasi-equilibrium tropical circulation model—Formulation. *J. Atmos. Sci.*, **57**, 1741–1766, https://doi.org/10.1175/1520-0469(2000)057<1741:AQETCM>2.0.CO;2.

Raymond, D. J., and Ž. Fuchs, 2009: Moisture modes and the Madden–Julian oscillation. *J. Climate*, **22**, 3031–3046, https://doi.org/10.1175/2008JCLI2739.1.

——, S. L. Sessions, and Ž. Fuchs, 2007: A theory for the spinup of tropical depressions. *Quart. J. Roy. Meteor. Soc.*, **133**, 1743–1754, https://doi.org/10.1002/qj.125.

——, ——, A. H. Sobel, and Ž. Fuchs, 2009: The mechanics of gross moist stability. *J. Adv. Model. Earth Syst.*, **1** (3), https://doi.org/10.3894/JAMES.2009.1.9.

——, ——, and C. López Carrillo, 2011: Thermodynamics of tropical cyclogenesis in the northwest Pacific. *J. Geophys. Res.*, **116**, D18101, https://doi.org/10.1029/2011JD015624.

——, Ž. Fuchs, S. Gjorgjievska, and S. Sessions, 2015: Balanced dynamics and convection in the tropical troposphere. *J. Adv. Model. Earth Syst.*, **7**, 1093–1116, https://doi.org/10.1002/2015MS000467.

Rushley, S. S., D. Kim, C. S. Bretherton, and M.-S. Ahn, 2018: Reexamining the nonlinear moisture-precipitation relationship over the tropical oceans. *Geophys. Res. Lett.*, **45**, 1133–1140, https://doi.org/10.1002/2017GL076296.

Rydbeck, A. V., and E. D. Maloney, 2015: On the convective coupling and moisture organization of east Pacific easterly waves. *J. Atmos. Sci.*, **72**, 3850–3870, https://doi.org/10.1175/JAS-D-15-0056.1.

——, ——, and G. J. Alaka Jr., 2017: In situ initiation of east Pacific easterly waves in a regional model. *J. Atmos. Sci.*, **74**, 333–351, https://doi.org/10.1175/JAS-D-16-0124.1.

Salvekar, P. S., L. George, and S. K. Mishra, 1986: Low level wind shear and baroclinic growth of monsoon depression scale waves. *Meteor. Atmos. Phys.*, **35**, 10–18, https://doi.org/10.1007/BF01029520.

Sanders, F., 1984: Quasi-geostrophic diagnosis of the monsoon depression of 5–8 July 1979. *J. Atmos. Sci.*, **41**, 538–552, https://doi.org/10.1175/1520-0469(1984)041<0538:QGDOTM>2.0.CO;2.

Sardeshmukh, P. D., and B. J. Hoskins, 1988: The generation of global rotational flow by steady idealized tropical divergence. *J. Atmos. Sci.*, **45**, 1228–1251, https://doi.org/10.1175/1520-0469(1988)045<1228:TGOGRF>2.0.CO;2.

Serra, Y. L., G. N. Kiladis, and M. F. Cronin, 2008: Horizontal and vertical structure of easterly waves in the Pacific ITCZ. *J. Atmos. Sci.*, **65**, 1266–1284, https://doi.org/10.1175/2007JAS2341.1.

Sikka, D. R., 1977: Some aspects of the life history, structure and movement of monsoon depressions. *Pure Appl. Geophys. (PAGEOPH)*, **115**, 1501–1529, https://doi.org/10.1007/BF00874421.

Smith, L. M., and S. N. Stechmann, 2017: Precipitating quasi-geostrophic equations and potential vorticity inversion with phase changes. *J. Atmos. Sci.*, **74**, 3285–3303, https://doi.org/10.1175/JAS-D-17-0023.1.

Snyder, C., and R. S. Lindzen, 1991: Quasi-geostrophic wave-CISK in an unbounded baroclinic shear. *J. Atmos. Sci.*, **48**, 76–86, https://doi.org/10.1175/1520-0469(1991)048<0076:QGWCIA>2.0.CO;2.

Sobel, A. H., 2002: Water vapor as an active scalar in tropical atmospheric dynamics. *Chaos*, **12**, 451–459, https://doi.org/10.1063/1.1480795.

——, and E. Maloney, 2012: An idealized semi-empirical framework for modeling the Madden–Julian oscillation. *J. Atmos. Sci.*, **69**, 1691–1705, https://doi.org/10.1175/JAS-D-11-0118.1.

——, and ——, 2013: Moisture modes and the eastward propagation of the MJO. *J. Atmos. Sci.*, **70**, 187–192, https://doi.org/10.1175/JAS-D-12-0189.1.

——, J. Nilsson, and L. M. Polvani, 2001: The weak temperature gradient approximation and balanced tropical moisture waves. *J. Atmos. Sci.*, **58**, 3650–3665, https://doi.org/10.1175/1520-0469(2001)058<3650:TWTGAA>2.0.CO;2.

Stano, G., T. N. Krishnamurti, T. S. V. V. Kumar, and A. Chakraborty, 2002: Hydrometeor structure of a composite monsoon depression using the TRMM radar. *Tellus*, **54A**, 370–381, https://doi.org/10.1034/j.1600-0870.2002.01330.x.

Subrahmanyam, D., M. K. Tandon, L. George, and S. K. Mishra, 1981: Role of barotropic mechanism in the development of a monsoon depression: A MONEX study. *Pure Appl. Geophys. (PAGEOPH)*, **119**, 901–912, https://doi.org/10.1007/BF00878958.

Sugiyama, M., 2009: The moisture mode in the quasi-equilibrium tropical circulation model. Part I: Analysis based on the weak temperature gradient approximation. *J. Atmos. Sci.*, **66**, 1507–1523, https://doi.org/10.1175/2008JAS2690.1.

Sukhatme, J., 2014: Low-frequency modes in an equatorial shallow-water model with moisture gradients. *Quart. J. Roy. Meteor. Soc.*, **140**, 1838–1846, https://doi.org/10.1002/qj.2264.

Vallis, G. K., 2017: *Atmospheric and Oceanic Fluid Dynamics*. Cambridge University Press, 964 pp.

Wallace, J. M., and P. V. Hobbs, 2006: *Atmospheric Science: An Introductory Survey*. 2nd ed. International Geophysics Series, Vol. 92. Academic Press, 504 pp.

Wang, B., and X. Xie, 1996: Low-frequency equatorial waves in vertically sheared zonal flow. Part I: Stable waves. *J. Atmos. Sci.*, **53**, 449–467, https://doi.org/10.1175/1520-0469(1996)053<0449:LFEWIV>2.0.CO;2.

Yanai, M., and T. Nitta, 1967: Computation of vertical motion and vorticity budget in a Caribbean easterly wave. *J. Meteor. Soc. Japan*, **45**, 444–466, https://doi.org/10.2151/jmsj1965.45.6_444.

——, S. Esbensen, and J. Chu, 1973: Determination of bulk properties of tropical cloud clusters from large-scale heat and moisture budgets. *J. Atmos. Sci.*, **30**, 611–627, https://doi.org/10.1175/1520-0469(1973)030<0611:DOBPOT>2.0.CO;2.

Yano, J.-I., and M. Bonazzola, 2009: Scale analysis for large-scale tropical atmospheric dynamics. *J. Atmos. Sci.*, **66**, 159–172, https://doi.org/10.1175/2008JAS2687.1.

Yoon, J.-H., and T.-C. Chen, 2005: Water vapor budget of the Indian monsoon depression. *Tellus*, **57A**, 770–782, https://doi.org/10.3402/tellusa.v57i5.14737.

——, and W.-R. Huang, 2012: Indian monsoon depression: Climatology and variability. *Modern Climatology*, InTech, 45–72.